3D PRINTING ENABLED STRUCTURAL COMPOSITES – FABRICATION, TESTING, AND NUMERICAL ANALYSIS

A Dissertation

by

YI-TANG KAO

Submitted to the Office of Graduate and Professional Studies of
Texas A&M University
in partial fulfillment of the requirements for the degree of

DOCTOR OF PHILOSOPHY

Chair of Committee,	Bruce L. Tai
Committee Members,	Jyhwen Wang
	Zhijian Pei
	Harry Hogan
	Terry Creasy
Head of Department,	Andreas Polycarpou

December 2019

Major Subject: Mechanical Engineering

ABSTRACT

This work introduces a structural composite material enabled by 3D printing technologies. The composite consists of a 3D-printed frame filled with another material for property enhancement. Unlike traditional composites that are designed by volume ratio and 2D structure (i.e., laminate orientation), the 3D printed composite can be built in a complex 3D configuration, such as lattice and honeycomb. In addition, instead of being a reinforced composite, the 3D printed composite is more like a dual-function material provided by two distinct phases. In this study, two types of the composite are developed and analyzed. The *type I* composite consists of a 3D printed brittle frame filled with a hyperelastic material, aimed for enhanced structural toughness. The *type II* composite consists of a 3D printed ductile frame filled with a viscoelastic foam for an enhanced impact resistivity. The objectives of this research are developing manufacturing methods for these composites by using both additive and molding processes, conducting experiments to evaluate the mechanical properties, and establishing numerical models to describe the mechanical behaviors and damage modes. The results show that both of the volume ratio and structural configuration determine the mechanical properties of the composite. For *type I* composite, the 3D printed brittle frame dominates the stiffness and the strength, and the hyperelastic material provides the toughness. Both experimental and numerical studies show that *type I* composite does not rupture suddenly under quasi-static bending test. This is because of the gradual development of the microcracks in the brittle frame as a result of contraction force provided by the hyperelastic filler. An FEA method includes a brittle cracking and a hyperelastic model successfully captures the bending behavior of *type I*

composite. Comparing to other conventional FEA models, this model enabled the analysis with coarse and uniform mesh in the structure to represent the crack evolution inside the material. *Type II* composite is tested under the low-velocity impact condition. The experimental results show that different foams affect the impact properties differently and do not necessarily show the improvement. The flexible foam can enhance the material ductility, absorb more energy, and slow down the crack propagation speed during the impact. An FEA method includes an elastoplastic and a viscoelastic model successfully represent the impact behaviors of the *type II* composite. The FEA results suggest that the foam reinforcement redistributes the stress and mitigates stress concentrations during impact. Consequently, the foam reinforcement enhances the material ductility without changing the structural stiffness and weight significantly.

ACKNOWLEDGEMENTS

I would like to thank my committee chair, Dr. Tai and my committee members, Dr. Wang, Dr. Pei, Dr. Hogan, and Dr. Creasy for their guidance and support throughout the course of this research.

Thanks also goes to all the members of the Manufacturing Innovation lab, my friends, and department faculties and staffs for making my time at Texas A&M University a great experience.

Lastly, thanks to my family for their support, motivation and love.

CONTRIBUTORS AND FUNDING SOURCES

Contributors

This work was supervised by a dissertation committee consisting of Assistant Professor Dr. Bruce Tai (Advisor) of the Department of Mechanical Engineering, Professor Dr. Jyhwen Wang of the Department of Engineering Technology and Industrial Distribution, Professor Dr. Zhijian Pei of the Department of Industrial & Systems Engineering, Professor Dr. Harry Hogan of the Department of Mechanical Engineering, and Associate Professor Dr. Terry Creasy of the Department of Materials Science & Engineering.

Part of the experiments in this dissertation was assisted by the members of the Manufacturing Innovation Lab.

Funding Sources

This study was supported by funding provided by NSF grant #1522877. Its contents are solely the responsibility of the authors and do not necessarily represent the official views of the NSF.

TABLE OF CONTENTS

Page

ABSTRACT ii

ACKNOWLEDGEMENTS iv

CONTRIBUTORS AND FUNDING SOURCES v

TABLE OF CONTENTS vi

LIST OF FIGURES viii

LIST OF TABLES xii

1. INTRODUCTION 1

1.1. Background 1
1.2. Literature Review 2
1.3. Research Objectives 4
1.4. Organization of the Dissertation 4

2. BENDING BEHAVIORS OF TYPE I COMPOSITE – EXPERIMENTAL STUDY. 5

2.1. Introduction 6
2.2. Materials and Methods 8
2.3. Experimental Results 11
2.4. Discussion 20
2.5. Conclusions 22

3. BENDING BEHAVIORS OF TYPE I COMPOSITE – NUMERICAL STUDY 24

3.1. Introduction 24
3.2. Finite Element Model Setup 25
3.3. Brittle Cracking Model 27
3.4. Model Parameters 29
3.5. FEA and Experiment Comparisons 33
3.6. *Type I* Composite Damage Conditions 35
3.7. Model Limitations 37
3.8. Conclusions 38

4. LOW-VELOCITY IMPACT BEHAVIORS OF TYPE II COMPOSITE – EXPERIMENTAL STUDY 39

4.1. Introduction 40
4.2. Materials and Methods 41
4.3. Experimental Results 49
4.4. Discussion 56
4.5. Conclusion 60

5. LOW-VELOCITY IMPACT BEHAVIORS OF TYPE II COMPOSITE – NUMERICAL STUDY 61

5.1. Introduction 61
5.2. Model setup and parameters 63
5.3. Model sensitivity analysis 71
5.4. Model results and comparison with experimental data 74
5.5. Model limitations 85
5.6. Conclusions 86

6. CONCLUSIONS AND FUTURE WORK 87

6.1. Conclusions and Major Contributions 87
6.2. Future Works 90

REFERENCES 92

LIST OF FIGURES

Page

Figure 1 Sample design: (a) the unit cell and assembly and (b) manufactured *type I* composite samples. 9

Figure 2 The mold for fabricating the composite samples 10

Figure 3 Four-point bending test setup 11

Figure 4 The force-deflection data of (a) *50S type I* composite, $50S_0$ pure plaster structure, and plaster-silicone material mixture; (b) *50L type I* composite, $50L_0$ pure plaster structure, and plaster-silicone material mixture 13

Figure 5 Tested *type I* composite samples with visible cracks in the plaster phase....14

Figure 6 Results for (a) 75L, (b) 75S, (c) 50L, and (d) 50S. Blue – cycle 1, red-cycle 2, green – cycle 3, and purple – cycle 4. Solid line and dashed line represent two repeated test....18

Figure 7 Changes of stiffness in each cycle for all four samples 19

Figure 8 Explanation of linear and nonlinear behaviors 21

Figure 9 Tested samples with cracks visible in the brittle phase 21

Figure 10 FEA model configuration for bending behavior simulation of *type I* composite 26

Figure 11 Four parameters for the brittle cracking model and their representations of element status within in each region 28

Figure 12 A non-linear four-point bending data and its correlations to brittle cracking model parameters 30

Figure 13 Inverse method and validation results for both $50S_0$ and $50L_0$ under (a) four-point bending and (b) three-point bending 32

Figure 14 The fitting result of the hyperelastic model using Marlow strain energy function 33

Figure 15 Experimental and FEA results of *type I* composite under four-point bending: (a) *50S* and (b) *50L* 34

Figure 16 Visualization of FEA results for *type I* composite behaviors under four-point bending 36

Figure 17 Simulated stress distributions of the silicone phase (a) without the constraint of the plaster structure (b) with the constraint of the plaster structure 37

Figure 18 *Type II* composite fabrication: (a) the unit-cell design and (b) the molding method 42

Figure 19 Manufactured *type II* composite samples with three different types of PU foams.....42

Figure 20 Manufactured tensile test samples 43

Figure 21 Design and actual setup of the drop-weight impact test 45

Figure 22 An example of data processing: (a) acceleration-time curve and (b) force-displacement curve 47

Figure 23 Maximum displacement of *type II* composite samples. * represents a statistical significance ($p < 0.05$) compared to pure *type II* frame. 50

Figure 24 Energy absorption of *type II* composite samples. * represents a statistical significance ($p < 0.05$) compared to pure *type II* frame. 51

Figure 25 Maximum acceleration of *type II* composite samples. * represents a statistical significance ($p < 0.05$) compared to pure *type II* frame. 52

Figure 26 Jerk of *type II* composite samples. * represents a statistical significance ($p < 0.05$) compared to pure *type II* frame.....53

Figure 27 High-speed images at different instantaneous times during impact for *type II* composite *with* (a) *FF-17* (b) *FF-25* (c) *FI-8* and (d) pure *type II* frame 54

Figure 28 Time duration of impact (a) from contact to crack initiation (b) from crack initiation to failure. * represents a statistical significance ($p < 0.05$) compared to pure *type II* frame.....55

Figure 29 Samples of *type II* composite with FF-17, sandwich structure, and solid PLA bar.....58

Figure 30 Comparisons of impact results among *type II* composite, sandwich structure, and solid PLA: (a) Jerk (b) Maximum displacement (c) Energy absorption and (d) Maximum acceleration 59

Figure 31 (a) 3D printed PLA frame and composite (b) the drop-weight impact test setup 64

Figure 32 FEA model configuration for *type II* composite 65

Figure 33 The strain rate effect of the PLA structure under 3-point bending test 66

Figure 34 The FEA model configuration for 3D printed frame 68

Figure 35 High speed images of 3D printed PLA frame at the initial failure 68

Figure 36 The comparison between the FEA and experiment three-point bending test 69

Figure 37 The comparison between the relaxation test and the curve fitting result 70

Figure 38 The mesh convergence test of the *type II* composite model 72

Figure 39 The compressive yield strength scaling factor sensitivity test of the 3D printed PLA lattice structural model 73

Figure 40 The sensitivity test of the PU foam's Poisson's ratio 74

Figure 41 Acceleration-time curves (a) 3D printed PLA lattice structure (b) *type II* composite 76

Figure 42 The maximum deflection of the *type II* composite and the PLA lattice structure 78

Figure 43 The maximum acceleration of the *type II* composite and the PLA lattice structure 79

Figure 44 The energy absorption of the *type II* composite and the PLA lattice structure 80

Figure 45 The jerk of the *type II* composite and the PLA lattice structure 81

Figure 46 (a) The definition of initial bending stage and the point right before the fracture (b) the definition of front view and bottom view 82

Figure 47 The stress distribution under the initial impact (a) *Type II* composite – front view (b) *Type II* composite – bottom view (c) PLA lattice structure – front view (d) PLA lattice structure – bottom view 83

Figure 48 Mechanical responses of the composite material (a) the foam material part inside the *type II* composite (b) the PLA lattice frame part inside the *type II* composite.....84

Figure 49 The stress distribution immediately before the fracture (a) *Type II* composite – front view (b) T*ype II* composite – bottom view (c) PLA lattice structure – front view (d) PLA lattice structure – bottom view.....85

LIST OF TABLES

Page

Table 1 The material parameters obtained from the inverse method 31

Table 2 Mechanical properties of the materials determined by the uniaxial tension 44

Table 3 The obtained parameters of the Maxwell model 70

1. INTRODUCTION

1.1. Background

Additive manufacturing, also known as 3D printing, is a manufacturing method that creates objects based on layer-by-layer deposition. Additive manufacturing has many advantages over the traditional, subtractive manufacturing, such as the ability to build the complex geometries and internal structures. Recent technology is being developed for high-performance applications with the emphases on functionality and durability [1, 2]. One major direction is toward 3D printed composite materials [3, 4]. 3D-printed composite materials can be made by material mixtures, which could be powders, polymer resins, or solid filaments, depending on the printing technologies such as Fused Deposition Modeling (FDM) [5, 6], Three-Dimensional Printing (3DP) [7-9], and Stereolithography (SLA) [10, 11]. Another type of composite is using a multi-feeding system to create a structural mixture during printing, such as combined powder and wire systems to create layers of different materials [12, 13]. In comparison, the material mixture blends materials homogeneously, whereas the structural mixture combines materials on a larger scale. The structural mixture allows the flexibility in design for different mechanical behaviors. An analogy is the reinforced concrete, where the concrete has high compression strength to carry the compressive load, and the rebars have the high tensile strength to carry the tension.

The objective of this dissertation is to create a structural composite that has a wide design domain and can be produced by 3D printing. Composite materials have become increasingly popular during the past decades. Particularly in engineering applications,

composite materials are sometimes preferable because of their high specific strength, stiffness, excellent corrosion resistance, improved fatigue resistance, or other enhanced properties towards a specific application. In traditional structural composites, engineers have worked on optimizing the honeycomb or laminated structures to improve and customize the properties of the composite materials [14]. With the emergence of additive manufacturing technologies, more complex structures other than honeycombs and laminates have become feasible, even with various material options. This research proposes a structural composite in a lattice configuration. Two types of composites are presented: *type I* composite is a brittle frame with a hyperelastic filler; *type II* composite is a ductile frame with a viscoelastic filler. This dissertation includes manufacturing methods for composite and investigations of their mechanical behaviors by using both experimental and numerical methods.

1.2. Literature Review

Brittle materials typically have a high stiffness but a low toughness, so a high safety factor is usually used in engineering design. To enhance the properties of brittle materials, studies have shown that adding ductile particles can prevent the sudden fracture. L. S. Sigl et al. [15] showed that the brittle material combine with a ductile phase could have a plastic stretching mechanism. This mechanism can significantly prevent the material fracture at the sudden. P.A. Mataga [16] developed a numerical model to show the toughness enhancement after adding a ductile phase into a brittle material. Hao Wu et al. [17] studied the fracture phenomena of the brittle-ductile multilayered composites. The results showed a good strength-ductility combination after the design of the laminated structure.

However, the ductile phase in these studies is either randomly distributed or in a simple 2D configuration. The effect of toughness enhancement may be limited. In comparison, *type I* composite incorporates the structural design of both phases and can be controlled more quantitatively.

The ductile materials like polymers and metals are common engineering materials, but they may behave brittle under high-strain-rate loads or impacts. To increase the impact resistance, researchers have combined different materials to create a composite material or optimized the structure inside the composite material, such as changing the laminate orientation or honeycomb structure. Zhang et al. [18] presented an idea of the structural composite using a polyurethane-foam-filled pyramidal lattice. The results showed that the specimen with foam-filled core had a significant improvement of energy absorption in compression tests compared to those with an unfilled core, but the improvement in impact tests was little. Jeremy Gustin et al. [19] studied the foam filled sandwich composites under low-velocity impact testing. The experimental results define the benefits of replacing carbon fiber layers with Kevlar or hybrid on the top and bottom layers. M.V. Hosur et al. [20] developed a foam-filled 3D integrated core sandwich composite laminates. The results show that the material has a great potential for structural application by providing additional layer at the top and bottom. However, the composite with special structural design requires complex manufacturing methods, such as slot-fitting and adhesive method [18, 21, 22], extrusion and electrical discharge machining [23], or a perforating technique [24, 25]. By using 3D printing technologies, it can significantly reduce the effort for the manufacturing process, and provides more material options

compared to traditional manufacturing. The *type II* composite, in this study, is with a 3D printed lattice frame filled with a viscoelastic foam for enhanced impact properties.

1.3. Research Objectives

The objective of this research is to develop manufacturing methods for both *type I* and *type II* composite and determine their mechanical behaviors using both experimental and numerical methods. The numerical analysis will be conducted using finite element method, aimed at understanding the damage phenomena of composite, and thus it can be used as a tool for the future design. The ultimate goal of this research is to enable an optimal design of composite for various engineering applications.

1.4. Organization of the Dissertation

This dissertation follows the regular journal format. Each chapter has abstract, introduction, materials & methods, results, discussions, and conclusions. Chapter 2 discusses the experimental study of *type I* composite, including four-point bending test and loading-unloading test. Chapter 3 presents the finite element analysis (FEA) study of the *type I* composite under quasi-static bending condition. Chapter 4 details the experimental study of the *type II* composite under low-velocity impact test. Chapter 5 shows the FEA study of the *type II* composite and explain the foam reinforcement effect in the material. In the end, chapter 6 concludes the dissertation and propose future works for this topic.

2. BENDING BEHAVIORS OF TYPE I COMPOSITE – EXPERIMENTAL STUDY*

This chapter* investigates the bending behaviors of *type I* composite using the experimental method. The *type I* composite is a composite material built by a 3D-printed brittle plaster lattice structure and filled with a silicone elastomer. The material composition and structural configuration of the two materials determine the overall mechanical properties. Four-point bending test results show a non-linear elastic property, and enhanced toughness and strength of *type I* composite samples compared to either material phase alone. Such behavior is believed to be a result of delayed microcrack propagation in the brittle phase and a hardening effect of elastomer. Four-point bending tests with loading-unloading cycles of preceding deformations were also conducted. The results show that there exists a linear–nonlinear transition when the bending deflection is around 2 mm in the first cycle bending. As the cycle proceeds, this linear–nonlinear transition is found at the maximum deflection of the previous cycle; meanwhile, the bending stiffness degrades. It is believed that the occurrence of microcracks inside the plaster frame is the mechanism behind the phenomenon. The silicone provides a strong network suppressing the abrupt crack propagation in a brittle

---

* Reprinted with permission from "Bending behaviors of 3D-printed Bi-material structure: Experimental study and finite element analysis." Kao, Y. T., Zhang, Y., Wang, J., & Tai, B. L., 2017, *Additive Manufacturing*, *16*, 197-205. Copyright 2017 by Elsevier B.V.

* Reprinted with permission from "Loading–Unloading Cycles of Three-Dimensional-Printed Built Bimaterial Structures with Ceramic and Elastomer. " Kao, Y. T., Zhang, Y., Wang, J., & Tai, B. L., 2017, *Journal of Manufacturing Science and Engineering*, *139*(4), 041006. Copyright 2017 by ASME.

material. The effects of the frame structure and plaster–silicone ratio were also compared. A high plaster content and large cell size tend to have higher stiffness and obvious linear to nonlinear transition while it also has more significant stiffness degradation.

2.1. Introduction

Additive manufacturing (AM) technologies provide the possibility to create complicated geometry based on layer-by-layer fabrication [26]. The recent development of AM is aiming toward high-precision and high-performance applications, one of which is developing multiple-material 3D printing, also known as composites [3]. AM of composites can be realized by fused deposition modeling (FDM) [5, 6], selective laser sintering/melting (SLS/SLM) [4, 27], laminated object manufacturing (LOM) [28], and laser engineered net shape (LENS) [29]. These studies use the preprepared mixtures of the composite materials, such as the mixed powder materials for SLS and the mixed filament for FDM. For example, Chung and Das [30] studied functionally graded materials by using a commercially available SLS machine. On the other hand, some other techniques manufacture composites using multiple feeding systems. For example, Wang et al. [12] used direct laser fabrication (DLF) technique to create Ti-6Al-4V reinforced with TiC. The composite material was manufactured by both wire and powder systems. Krishna et al. [31] presented an experimental study of a functionally graded Co–Cr–Mo coating on Ti-6Al-4V alloy by using LENS with double powder feeder system. To be noted that the majority of the existing AM methods for composites are based on material mixtures. This chapter, in contrast, focuses on AM of the composite using structural mixture rather than the material mixture.

The structural mixture here refers to a larger scale of mixing between two or multiple materials, such as honeycomb or laminates composite. The mechanical behaviors of these materials are affected by both the material composition and the structural configuration. The produced part, therefore, can be designed structurally for specific needs, such as localized strength or anisotropy property. The two selected materials for *type I* composite are ceramic and elastomer due to the brittle and hyperelastic natures, respectively, that potentially provide both strength and toughness to the structure.

Conventional materials, such as metals or plastics, usually have a constant modulus of elasticity in the elastic region or when reloaded in the plastic region. Thus, the resilience (i.e., the elastic strain energy absorbed by the material) remains similar despite the deformation magnitude. The *type I* composite is anticipated to have varying stiffness and resilience due to the elastic nature of both materials and the stiffness degradation phenomenon. Stiff degradation is a result of microdamages in one of the phases (usually the more brittle one) inside the composites. Gagel et al. [32] showed that the stiffness degradation occurs on glass-fiber reinforced epoxy material by loading–unloading cycles experiment. Lee and Fenves [33] reported a model to explain the stiffness degradation of concrete structures. Flores-Johnson et al. [34] presented a report for the degradation of stiffness on crushable foams in uniaxial compression. In general, when the stiffness degradation occurs, the material experiences a longer loading curve in the elastic region while it remains a similar maximum strength, which results in increasing resilience. This material is a compromise between resilience and stiffness.

This chapter, therefore, presents a concept of 3D printing technology that can construct a composite of not only multiple materials but also with selected structural strength. The proposed *type I* composite consists of two vastly different materials and thus possesses a broader range of mechanical properties (from brittle to ductile) that could be tailored by manufacturers. Furthermore, different geometrical arrangements of these two phases can create different directional strengths. This concept is similar to the reinforced concrete used in construction with concrete as a rigid base and rebar as a tough addition. Owing to the flexibility of 3D printing, the desired structure design can be easily fabricated. In this chapter, a conceptual prototype was made with a powder-bed printer for the brittle phase and then combined with a silicone material as the ductile phase. The objective is to experimentally measure the changes in mechanical properties of the built composite and determine the effects of composition and structure.

2.2. Materials and Methods

A four-point bending test was utilized to examine the material properties of the *type I* composite. The sample was designed to be 156 mm × 13 mm × 6.5 mm based on an open-cellular unit cubic structure to accommodate the silicone material, as shown in Fig. 1. The porosity of the part is determined by a unit cubic cell with a specific void-to-body ratio, and the unit cells are assembled to form the part, as shown in Fig.1 (a). The complementary percentage of this ratio is defined as the composition ratio. A different structure could be made with an identical composition ratio.

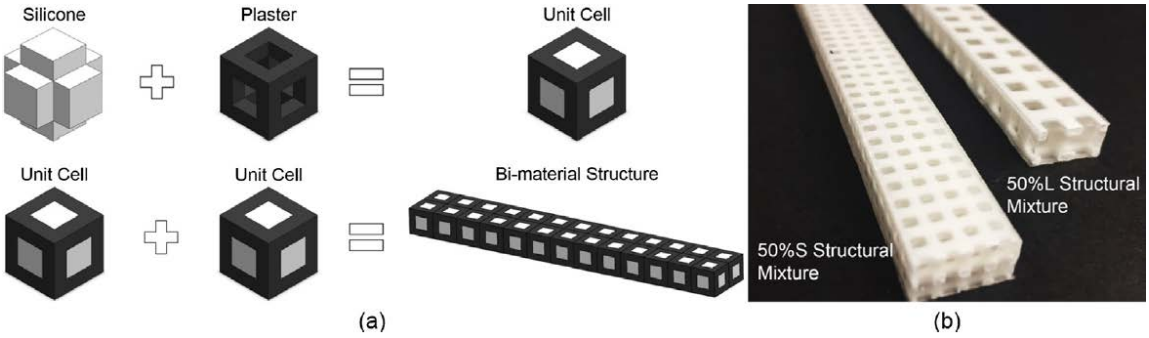

Figure 1 Sample design: (a) the unit cell and assembly and (b) manufactured *type I* composite samples. (Reprinted with permission from [35])

In this study, the term *50L* represents the samples with a 6.5 mm unit cell length and 50:50 mixing ratio; *50S* is made of the same volume fraction with a 3.25 mm unit cell length. These samples were manufactured using a binder jetting 3D printer, ProJet 160 (3D Systems, Rock Hill, SC), which builds plaster parts with a powder-bed technology. The powders are bonded with the designated chemical binder to fuse the plaster particles together. The binder, containing more than 90% water, does not produce any additional hardness and strength to the printed part. The silicone phase was Sylgard 184 (Dow Corning, Midland, MI) because of its low stiffness and good flowability (low viscosity) for casting and molding. The elastic modulus of the brittle frame was more than 100 times higher than that of the silicone, and thus the silicone is not expected to affect the overall bending stiffness. The silicone resin and the hardener were mixed at a 10:1 ratio and degassing in a vacuum chamber. Before the molding process, the 3D printed plaster frame was baked at 80 °C in an air oven for 5 min to take out the moisture absorbed from the environment. The mold for fabricating the *type I* composite is shown in Fig. 2. The molded samples were degassed again to remove the remaining air during the molding

process and then baked in the air oven at 50°C for 15 h in order to fully cure the materials. The produced samples are shown in Fig. 1 (b). In order to see the effect of the baking temperature, the samples used in the loading-unloading test was baked at 150°C for 2 h after the molding process.

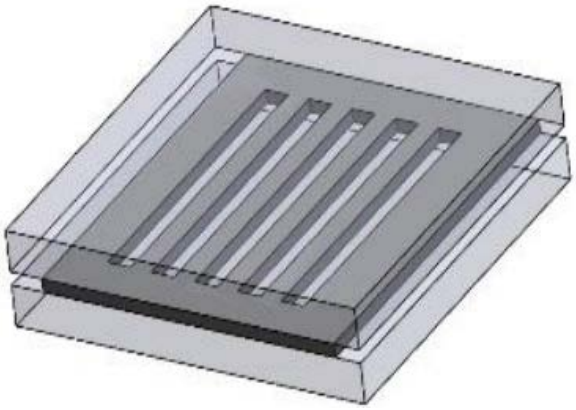

Figure 2 The mold for fabricating the composite samples

For the bending behavior characterization, as shown in Fig. 3, a standard four-point bending test following ASTM-D7264 [36] was utilized. The radius of the cylindrical contact surface for the loading and support noses were 5 mm, and the spans were 64 mm and 128 mm respectively. The displacement of the loading noses was controlled at the rate of 1.27 mm/min (0.05inches/min) throughout the test. The loading force and the loading nose displacement data were captured. The loading nose displacement is defined as deflection in this study since the deflection at the mid-point may not necessarily follow the Euler beam equation after the damage begins.

In addition to the bending test, loading–unloading tests were conducted on the same setup. Four loading-unloading cycles were applied on each sample. The deflection of the loading nose was 11.18 mm (0.44 in.) for first two cycles. To observe the linear–nonlinear behavior of the samples, the deflection distance was chosen from the bending results, which all the samples pass the elastic region in the force–deflection curves. For third and fourth cycles, the deflection distance was 22.35 mm (0.88 in.), which results were used to determine the effect of deflection level on linear–nonlinear behavior.

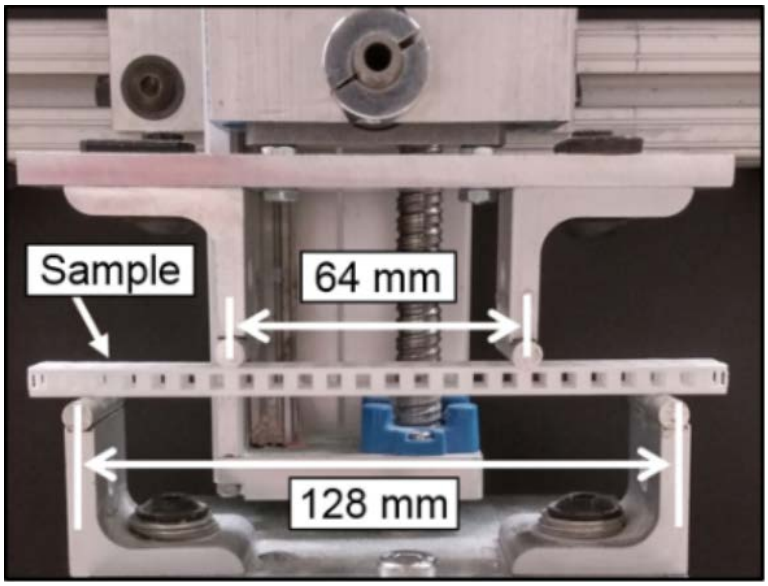

Figure 3 Four-point bending test setup (Reprinted with permission from [35])

2.3. Experimental Results

The force-deflection curves results of four-point bending tests are shown in Fig. 4 (a) and (b) for *50S* and *50L*, respectively. For the comparison purpose, the plaster structures without the silicone elastomer (denoted by $50S_0$ and $50\ L_0$) and a pure material mixture of

50:50 composition ratio were also plotted in the figure. As shown, the bending stiffness and the strength of the material mixture are considerably lower than those of the *type I* composite and the pure plaster structures. This is because the plaster powders in the material mixture act as a dispersion strengthening agent for the silicone matrix. However, for *type I* composite, the plaster structure produces the bending stiffness, and the silicone material provides the toughness.

In comparison between the pure plaster structures and *type I* composite, the bending stiffness is similar (about 11 N/mm for *50L* and 5 N/mm for *50S*) with and without the silicone filler, but the silicone avoid the fracture occurs in *type I* composite. Both structures deflect over 6 mm before rupture. Additionally, the maximum load carrying capability of *type I* composite, which is linearly proportional to the flexural strength, is higher than that of the pure plaster structure despite the silicone material having an extremely low modulus. However, the amount of increase in flexural strength is not as significant as that of the toughness. The results suggest that the bending stiffness and the flexural strength are primarily dominated by the plaster structure while the toughness is contributed by the silicone phase.

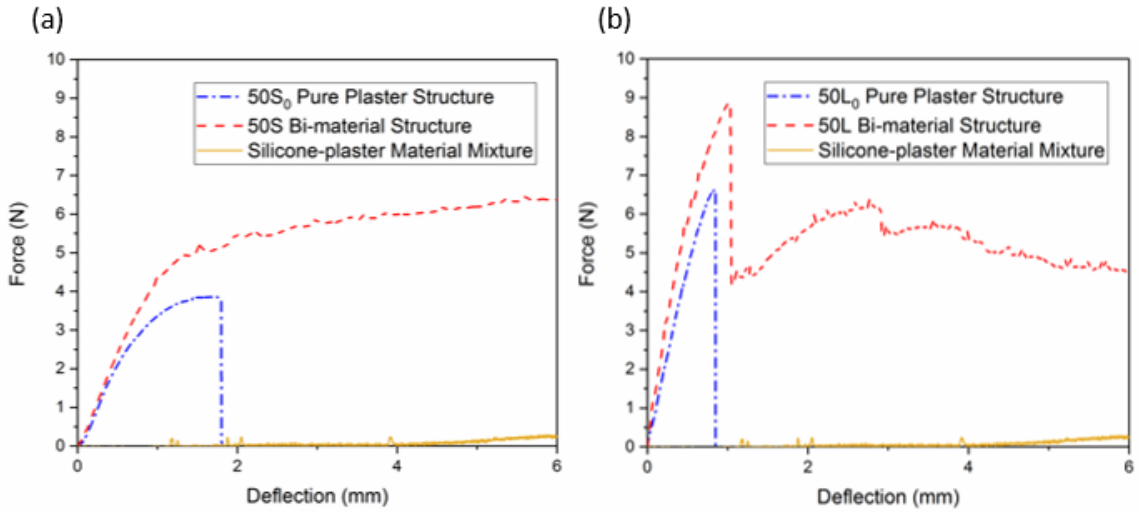

Figure 4 The force-deflection data of (a) *50S type I* composite, *50S*$_0$ pure plaster structure, and plaster-silicone material mixture; (b) *50L type I* composite, *50L*$_0$ pure plaster structure, and plaster-silicone material mixture (Reprinted with permission from [35])

In comparison between *50S* and *50L*, the bending stiffness of *50S* is constant till around 1.0 mm deflection and then starts to degrade, while the load carrying capability increases slowly. There is no significant structural failure through the test. The silicone phase prevents the structure from falling apart and strengthens the structure under a tri-axial stress. Note that the *50S*$_0$ sample (plaster structure only) has already failed when the deflection is around 2 mm. For the samples of *50L*, the force-deflection curve is linear at the beginning and exhibits a sudden force drop around 1 mm deflection. This noticeable change from the behavior *of 50S* is due to the structural difference in the plaster phase. The force drop indicates that there is significant structural damage but not a complete failure at this moment. The force increases afterward, and the specimen regains some load-carrying capability around 5 to 6 N. Secondary structural damage can be seen around 3

mm deflection, which represents additional structural damage in the plaster phase. Although the structure has been severely damaged, the cracks inside the plaster phase do not completely propagate to the opposing side, and the beam can still carry some load because of the holding force from the silicone.

Based on the results, it is believed that the hyperelastic property of the silicone plays an important role in maintaining the *type I* composite structural integrity under bending. The contraction of silicone prevents the microcracks from propagating easily through the structure. This is evidenced by visually observed cracks on the bottoms of both *50S* and *50L* samples under bending, as shown in Fig. 5. Moreover, the fine structure of *50S* confines the cracks on the bottom layer, so the structural remains a certain strength after significant bending. The coarse structure of *50L* allows cracks to propagate toward the neutral axis, which leads to a quick and severe structural damage as shown in the data.

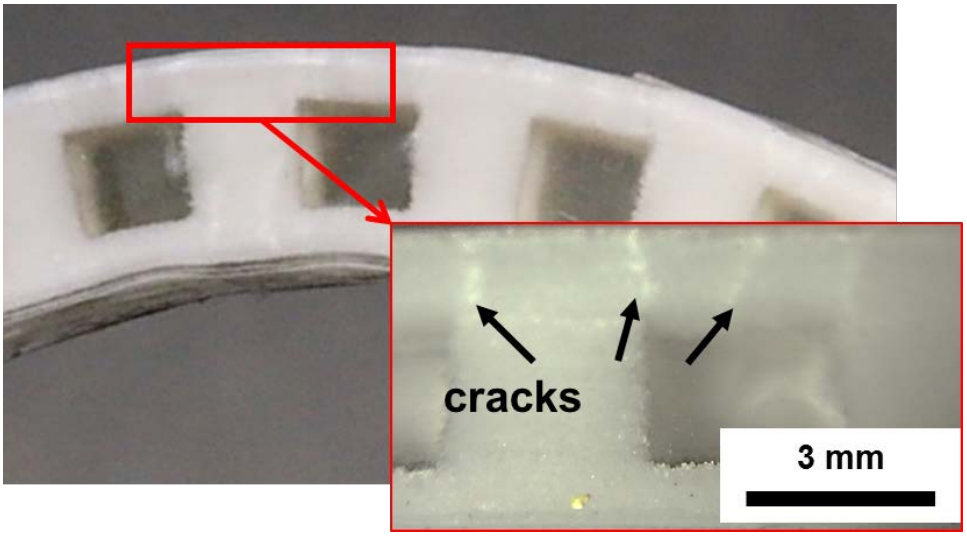

Figure 5 Tested *type I* composite samples with visible cracks in the plaster phase (Reprinted with permission from [35])

Figure 6 shows two repeated loading-unloading test results of all the samples used in this study. The solid line and the dashed line represent two separate test results. The force-deflection curves are almost identical throughout the whole process. This shows a high repeatability of the setup as well as the sample. All of them exhibit similar behavior during the test. For the first cycle, the structure deforms elastically at the beginning of the loading and the elastic region ends when the deflection of the sample is at about 2 mm. This transition point is approximated as it is sometimes unclear on where the point exactly is. When the deflection exceeds this transition point, the curve turns into a more plateau region, similar to the elastic-to-plastic transition, till the unloading begins. The unloading cycle recovers most of the deflection, but there is a small unrecovered deformation about 2 to 3 mm (point p). The recovery of the most of the deflection indicates that the transition point is a stiffness transition, instead of the yielding point; the material remains elastic beyond this point. The unrecovered deformation is due to there is no waiting time between the unloading and loading bending. It is believed that over a longer time, the material should recover to the original shape. This can be observed after the fourth loading cycle of the bending. For the second loading cycle, the force increases linearly when it reaches the previous unloading point (about 10 mm). The slope of the second loading is lower than the first one. This is an evidence of stiffness degradation. For the unloading part, the second unloading curve is similar to the first unloading curve. The second cycle behaves as to reveal a completely linear elastic deformation with a hysteresis effect, a common phenomenon in polymers.

The third loading cycle follows the linear trend till it reaches the maximum deflection of the previous cycles, and then, the sample again starts to deform nonlinearly. This behavior is almost identical to the first cycle except that the stiffness, unrecovered deformation, and transition points have changed. The unrecovered deformation is about 4 to 5 mm. This is higher than the second cycle, shown as point q in Fig. 6. The fourth cycle is similar to the second cycle, where loading curve shows a linear behavior and unloading curve exhibits slight material hysteresis.

Specifically, in 75L (Fig. 5a), the non-linear transition is relatively noticeable. The linear region extends straight to the 1.5 mm deflection level and turns into nonlinear deformation before it is unloaded. The maximum load remains around 4.5 N to 5 N as the deflection keeps increasing with the cycles. The second and fourth loadings both show a completely linear curve. In comparison, the transition of 75S (Fig. 5b) is not as clear as that of 75L. Also, the maximum load of 75S increases with the increasing deflection over the cycles. No plateau is observed. Therefore, the transition is at a higher force as the cycle proceeds, similar to the strain-hardening effect in the regular stress-strain curve. On the other hand, although the first transition points are not the same, they both land in somewhere between 1.5 mm and 2.5 mm. This implies that the defects (e.g., pores, flaws, cracks) start to take place at this deformation level regardless of the structural configuration. This is particularly true of the 75% structure when it is more dominated by the brittle plaster phase.

The 50% cases have a lower maximum force of each cycle than that of the 75% cases due to the plaster content, which dominates the strength of the structure. In addition, the

50% cases have more obvious “pseudo-strain” hardening effect, particularly for 50S. The maximum force of the non-linear transition increases significantly with the cycle (deflection). On the other hand, for a fixed plaster content (50% or 75%), the small cell size tends to have more the pseudo-strain hardening effect. These observations conclude that non-linear elastic transition behavior and the hardening effect are both affected by the content of plaster and silicone as well as the structure. The repeatability of loading and unloading curves also suggest a stable microstructure inside the material. To be noted that, the samples in the loading-unloading test does not showed a significantly drop (Fig. 4(b)), and the stiffness is significantly lower than the previous results. This indicates that the baking temperature has a significant effect on the material properties, and higher temperature tends to degrade the properties.

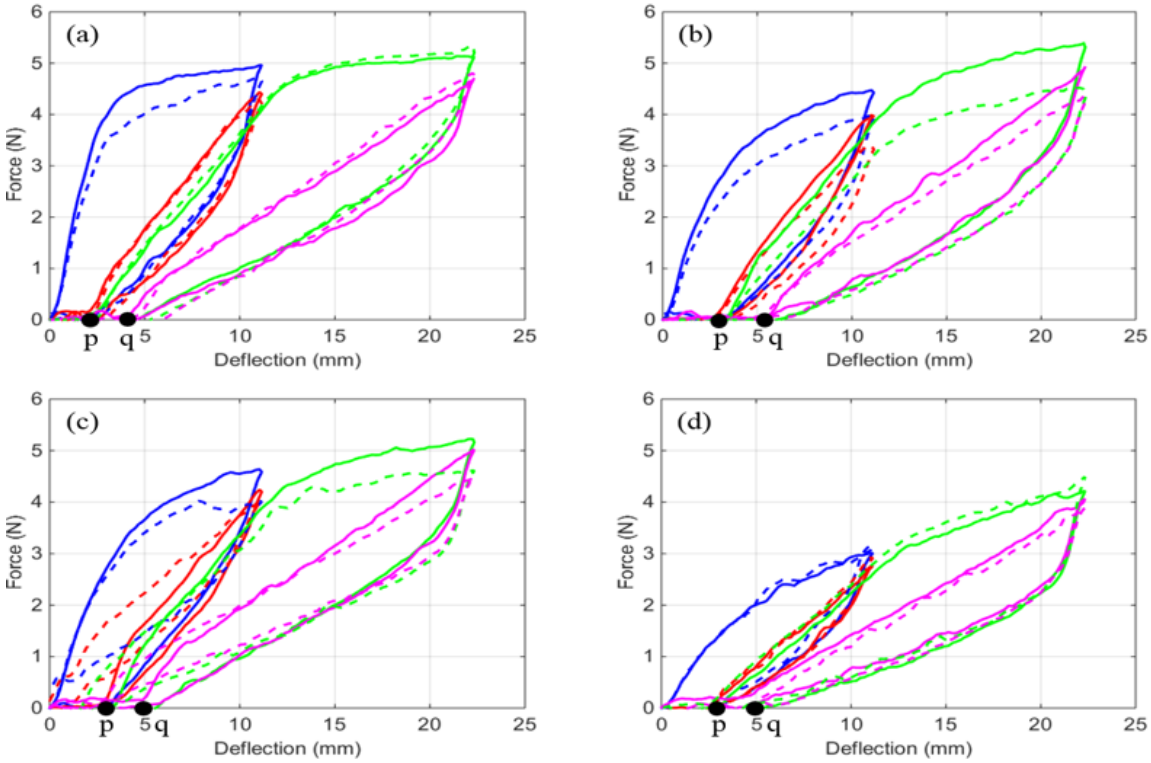

Figure 6 Results for (a) 75L, (b) 75S, (c) 50L, and (d) 50S. Blue – cycle 1, red- cycle 2, green – cycle 3, and purple – cycle 4. Solid line and dashed line represent two repeated test (Reprinted with permission from [37])

Figure 7 shows the comparison of the slope of the force-deflection curve for each cycle of all four cases. This slope in a linear elastic region represents the bending stiffness of the structure. Mathematically, the bending stiffness was calculated using the first 1 mm deflection data from the force starts to increase. Note there is unrecovered deflection for cycles 2 to 4. The comparison is based on two repeated tests of each case.

For all of the samples, the bending stiffness decreases after each cycle, and all of them show a similar trend for stiffness degradation. From the first cycle to the second cycle, the stiffness of every sample decreases around 50% to 60%. This is the highest degradation

in the whole test. From the second cycle to the third cycle, there is almost no stiffness degradation because no nonlinear deformation occurs in the second cycle. From the third cycle to the fourth cycle, the stiffness significantly decreases again. The amount of degradation is about 30% to 50%, which is less than the first degradation.

Specifically in each case, for the first cycle, 75L has the highest stiffness compared to the other cases. 75S and 50L have a similar stiffness of the first cycle, 50L is slightly lower than 75L but significantly higher than 50S. After the first cycle, the stiffness of the rest of three cycles become similar for 75L, 75S, and 50L cases. This implies that the level of the stiffness degradation of 75L is higher than 75S and 50L. In regards to 50S case, it shows the lowest stiffness for every cycle compared to all the other cases.

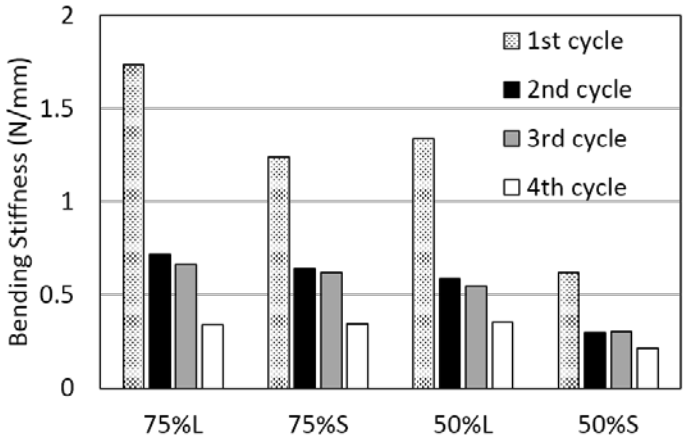

Figure 7 Changes of stiffness in each cycle for all four samples (Reprinted with permission from [37])

2.4. Discussion

According to the results, different compositions and structures lead to different behaviors during the bending test. The discussion is focused on how the non-linear elastic behavior forms and how the structural configuration affects these behaviors.

The material deforms elastically at the beginning of bending and turns to nonlinear deformation after certain deflection level. Figure 8 illustrates, via diagrams, a hypothesis to explain the phenomenon of the transition from linear to nonlinear elastic behavior. At the beginning of bending, the linear curve is because both materials (plaster and silicone) are elastic. When the deflection level reaches a certain threshold, the deflection of the material creates internal cracks inside the brittle phase. These cracks remain stable and do not propagate abruptly to the top since the surrounding structure is tightly secured by the silicone network (i.e. the orthogonal structure). However, as the cycle proceeds, the larger deflection creates more cracks in the structure, which decreases the stiffness of the samples. If the deflection level keeps increasing, the sample will eventually fail because the cracks completely destroy the integrity of the structure. Therefore, when the cracks start to appear in the material, the structure transitions from the linear behavior to the nonlinear behavior. Fig. 9 shows the tested sample after loading that contains internal cracks in the brittle phase.

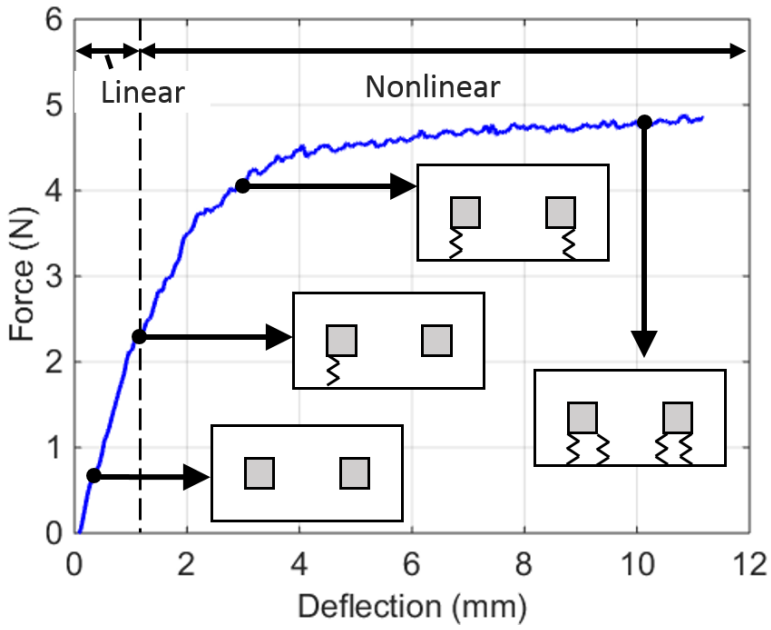

Figure 8 Explanation of linear and nonlinear behaviors (Reprinted with permission from [37])

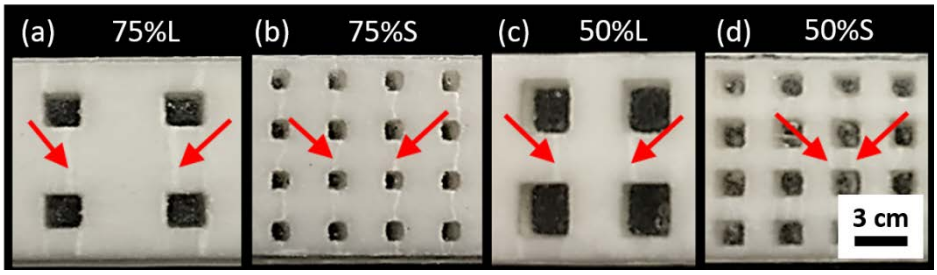

Figure 9 Tested samples with cracks visible in the brittle phase (Reprinted with permission from [37])

Stiffness degradation has been shown qualitatively and quantitatively in Figs. 6 and 7. This stiffness degradation is a result of the micro-cracks. Since the orthogonal structure of silicone can effectively secure the plaster and suppress (or slow down) the crack propagation, the elastic behavior is maintained during repetitive cycles. Although the

structure has internally cracked resulting in stiffness degradation, it is not considered failure since the strength does not decrease. Further, the second cycle causes very minimum stiffness degradation (Fig. 7). This provides further evidence in revealing the elastic property. However, as the deformation proceeds to the third cycle, more or larger cracks are produced and thus again, decreases the stiffness. This stiffness degradation phenomenon is expected to reach a threshold where the structure starts to fail.

Specifically in this study, the level of degradation is found dependent on the cell size and composition. The stiffness of the large cell structure samples degrades around 60% after the first cycle. However, the small cell samples only degrade 50%. Interestingly, despite large differences in stiffness of the first cycle, the stiffness of all samples tend to be more similar afterward. This could be specific to this combination of materials or the nature of such *type I* composite. Further investigations with numerical modeling and other materials would need to be conducted in the future.

2.5. Conclusions

This chapter describes the bending behaviors of 3D printed t*ype I* composite by using four-point bending test. *Type I* composite contains a 3D printed brittle plaster lattice structure filled with silicone elastomer. The plaster phase dominates the stiffness and the strength under bending; the elastomer enhances the toughness. The results suggested that the plaster phase did not rupture suddenly because of the gradual development of microcracks as a result of contraction force provided by the silicone filler. However, this might not always be the case in a thicker structure (e.g., 50L) since the cracks propagate

longer and can further degrade the material at a time. The configuration along with the material composition can significantly affect the mechanical behaviors of composite.

The mechanical behaviors of the *type I* composite are further tested under loading-unloading test. The results showed interesting non-linear elastic phenomenon and stiffness degradation. The potential application could be for structural components that require high fracture toughness or impact toughness.

The current data have suggested a basic trend for the *type I* composite under the loading-unloading study. Evolution of micro-cracks was hypothesized to be the key mechanism behind these phenomena. The continuation of this work will be focused on the FEA development shown in the next chapter.

3. BENDING BEHAVIORS OF TYPE I COMPOSITE – NUMERICAL STUDY*

This chapter* investigates the bending behaviors of a *type I* composite using numerical methods. Finite element analysis (FEA) is employed to verify the hypotheses made in the previous chapter. The FEA incorporates a brittle cracking material model for the plaster and a hyperelastic model for the silicone. The brittle cracking model enables the estimation of element degradation as a result of crack development and thus eliminates the need for the extremely refined mesh. Simulation result confirms the non-linear elastic transition and crack-induced material degradation and visualizes the silicone strengthening mechanism that can avoid rapid structural rupture.

3.1. Introduction

Composite materials can be modeled in various ways. Analytical models for the laminated or sandwich composite have been well developed [38-40], but they cannot be directly extended and applied to a complex 3D geometry. Representative elementary volume (REV) is another technique to analyze the mechanical behaviors of composite materials [41-43]. REV is the smallest volume that will yield to the real effective properties of the composite [44]. Tabiei and Jiang [45] used REV to simulate the mechanical behavior of the woven fabric composite material. Liu and Chen [46, 47]

* Reprinted with permission from "Bending behaviors of 3D-printed Bi-material structure: Experimental study and finite element analysis." Kao, Y. T., Zhang, Y., Wang, J., & Tai, B. L., 2017, *Additive Manufacturing*, *16*, 197-205. Copyright 2017 by Elsevier B.V.

evaluate the mechanical properties of carbon nanotubes composite using REV along with finite element analysis (FEA). Applying REV to the *type I* composite is possible but difficult to formulate the stiffness matrix because of a possibly inhomogeneous geometry. Therefore, another FEA method is used in this study to construct an exact geometry. The model uniquely employs a brittle cracking model [48] to simulate the frame structure and a hyperelastic model for the silicone elastomer. The brittle cracking model emulates the frame degradation due to crack generation under tension; the hyperelastic model describes the non-linear behavior of elastomer under a large strain.

To explain the phenomena observed in the experimental tests, a finite element analysis (FEA) model was built to verify the *type I* composite phenomenon of slowly propagated microcracks. A typical crack model requires very fine mesh and heavy computational power to capture the crack propagation and new surface interactions. Alternatively, this chapter attempts a unique model using a brittle cracking material setting that allows the relatively coarse mesh to achieve the same goal. The model setup and selection are detailed in the following sections.

3.2. Finite Element Model Setup

The FEA model was constructed using ABAQUS (Version 6.14-2) to simulate the bending behaviors of *type I* composite. Since the 4-point bending setup was symmetric in both X- and Z-directions, only a quarter of the sample was built to maximize the computational efficiency, as shown in Fig. 10. The model contained two material sections, plaster and silicone, with an ideal orthogonal cellular geometry. The printed geometrical errors were not taken into account. Symmetric faces were defined accordingly by fixing

the rotational and translational motions. The loading and support noses were rigid bodies that could contact all exterior surfaces (defined by GENERAL CONTACT). A small value of friction coefficient, μ = 0.01, between the specimen and loading/support noses was assumed. A hexagonal mesh (C3D8I) with 0.8125 mm cubic length was chosen for the model to fit four elements equally along the *50S* cell length and eight elements for the *50L*.

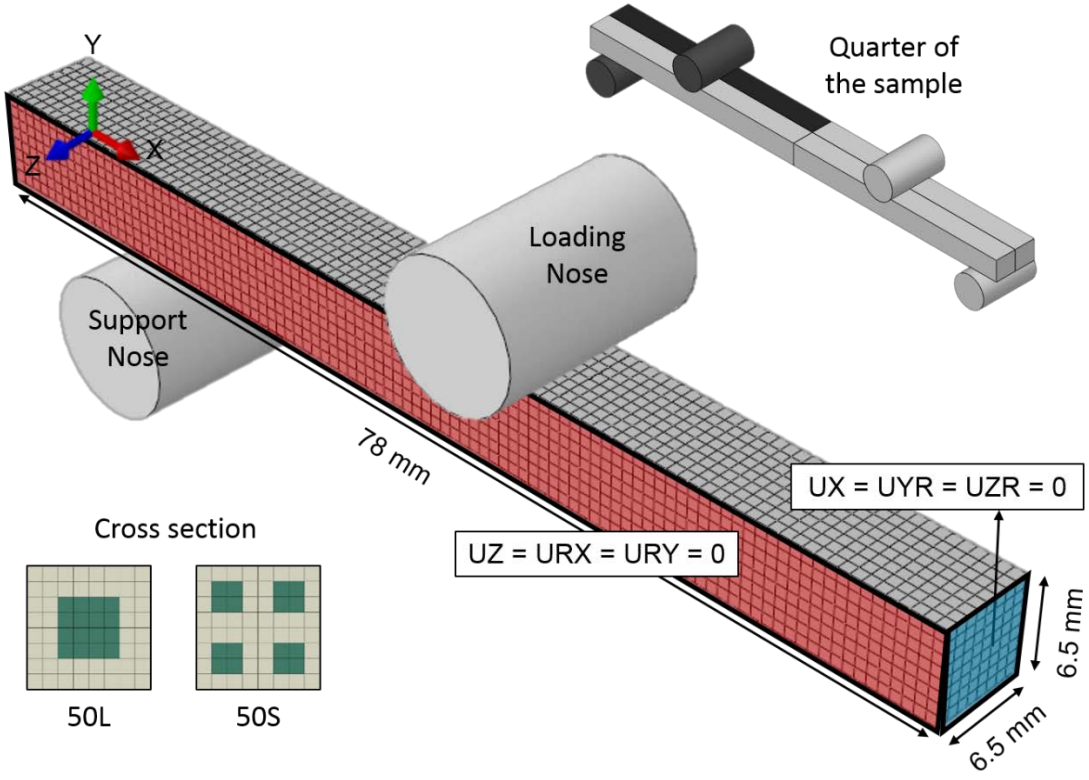

Figure 10 FEA model configuration for bending behavior simulation of *type I* composite (Reprinted with permission from[35])

The failure of the brittle material is generally attributed to the growth of microcracks [49]. These cracks initiate at a high tensile stress region and rapidly propagate through the

structure, leading to a sudden rupture. Conventionally, such phenomenon can be handled by two FEA methods. First, the model can mesh with extremely fine elements [50]. The small mesh size can capture the stress concentration at the crack tip, and the elements can be eliminated when the stress has reached the damage criteria. Also due to the fine mesh, the deletion of elements does not cause significant volume loss of the model; the crack can propagate freely within the modeling domain. However, the computational time can be significantly increased. The computational time is generally proportional to the number of elements [51, 52]. The other approach is using extended finite element method (XFEM). XFEM is primarily adopted for analyzing the crack propagation [53] based on the initial defects such as voids, cracks, or inhomogeneity in the material [54]. However, the initial defect conditions cannot be defined in the *type I* composite. Alternatively, this study utilized the BRITTLE CRACKING material model available in ABAQUS/EXPLICIT to simulate the brittle failure mechanism. This material model was originally developed to simulate the material degradation of concrete, ceramics, or brittle rocks [48, 55]. *Type I* composite has a degradation behavior similar to the aforementioned materials. As shown in the previous chapter, *type I* composite exhibits a reduced stiffness, while remaining elastic, under several loading and unloading cycles with an incremental deflection.

3.3. Brittle Cracking Model

The brittle cracking model is described schematically in Fig. 11 with four parameters, denoted by E, Y, D, and ε_R. The stress increases linearly with the strain at a slope of E till it reaches the yield point Y. Plastic deformation does not occur after the yield point; instead, the material begins to degrade at a rate of D as the strain continues to increase.

The degradation is not necessarily a linear behavior but was assumed a linear degradation in this study. This degradation area is called post-failure region, which emulates the occurrence of micro-cracks inside the material. Within this region, a shear-to-tensile ratio often needs to be defined to reflect the degradation of the shear strength as a function of tensile strength. This ratio was measured by a single shear test of the bulk plaster material and found to be around 50%. However, according to the numerical tests and other studies [56, 57], the bending behavior was insensitive to this parameter. Finally, the material ruptures at point ε_R since no more cracks can be carried and the structure disintegrates suddenly. Note the BRITTLE CRACKING model can only be damaged by tensile stress; the compressive behavior is assumed linear without damage. Although this is the model's constraint, it is almost always true that brittle materials have a much higher compression strength than tensile strength. The material should initiate tensile damages before the compressive stress reaches a critical level.

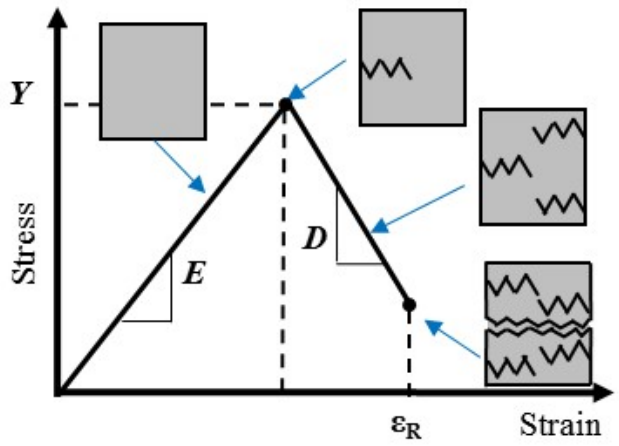

Figure 11 Four parameters for the brittle cracking model and their representations of element status within in each region (Reprinted with permission from[35])

These parameters may be measured directly from the bulk material properties, but the initial work found a significant deviation when the elastic modulus of the bulk material (100% printed plaster) was applied to simulate frame structures of *50S*, *50L*, *75S*, and *75L*. The deviation became noticeable, particularly when the feature size became smaller (e.g., the cross section area of the struts). Other mechanical properties, therefore, would also be different from the bulk material. This is, in fact, a common phenomenon in porous ceramic materials that pores or inherent defects affect the material properties more significantly when the size is small [58]. In this particular case, the smallest structural sizes (around 0.8 mm in *50S* and 1.6 mm for *50L*) are both close to the printer's resolution. To obtain an accurate set of parameters for analysis, an inverse method was used to extract the mechanical properties individually for each structure.

3.4. Model Parameters

The inverse method uses the data from the bending tests of *50S* and *50L* plaster frames (denoted by $50S_0$ and $50\ L_0$, respectively) to determine the four material parameters. This would have been a multi-variable optimization problem if these parameters were coupled together. A substantial convergence study then was needed to ensure the existence and uniqueness of the solutions [59]. Fortunately, in this study, it is possible to decompose these parameters into different sections of a force-deflection curve of a bending test. As shown in Fig. 12, the bending stiffness of the linear region is correspondent to the elastic modulus *E*. The linear region then transitions to a non-linear region where the degradation begins. The transition point is the elastic limit, correspondent to the yield point *Y*. The curve of the non-linear region is related to the degradation rate *D*. It is important to note

that this non-linear region is not the plastic deformation since the plaster is an elastic material. In the end, the specimen ruptures at a certain point where the force drops to zero. This rupture point is related to the failure strain ε_R.

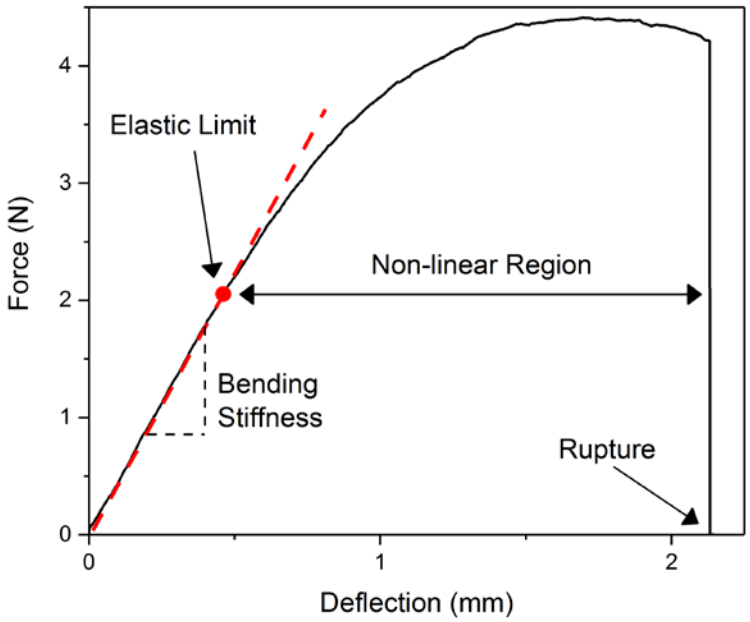

Figure 12 A non-linear four-point bending data and its correlations to brittle cracking model parameters (Reprinted with permission from[35])

Each parameter was searched using the Golden Section method individually within the corresponding section. A two-digit accuracy was utilized as the searching criterion. The objective function to be minimized was the cumulative discrepancy between the FEA and the experimental data within the selected section. One bending test was conducted as the input to find the parameters and another three replicas were conducted to ensure the model accuracy and the sample repeatability. The results obtained from the inverse method are shown in Table 1; the bending behaviors of $50L_0$ and $50S_0$ calculated using

these parameters are shown in Fig. 13 (a). The good agreements in the force-deflection behavior validated the use of the brittle crack model. The slight geometrical mismatch in the non-linear region of $50S_0$ is due to the setting of a constant D, which leads to a more bi-linear behavior. The differences of the rupture point are attributed to the material variations, such as defects and pores, among the testing replicas. Such an uncertainty especially is high when the feature size is small (i.e., $50S_0$). In additional to the four-point bending tests, three-point bending tests were also conducted to verify the parameters, as shown in Fig. 13 (b). There are some noticeable discrepancies in $50S_0$, but the overall behaviors are similar to the FEA results regarding the bending stiffness, linear-to-nonlinear transition, and the rupture point.

Table 1 The material parameters obtained from the inverse method (Reprinted with permission from[35])

Material Properties	*50S*	*50L*
Elastic Modulus (Mpa) (E)	780	1400
Yield Stress (Mpa) (Y)	1.4	1.9
Degradation Rate (Mpa) (D)	5.6	3.2
Failure Strain (ε_R)	0.2	0.03

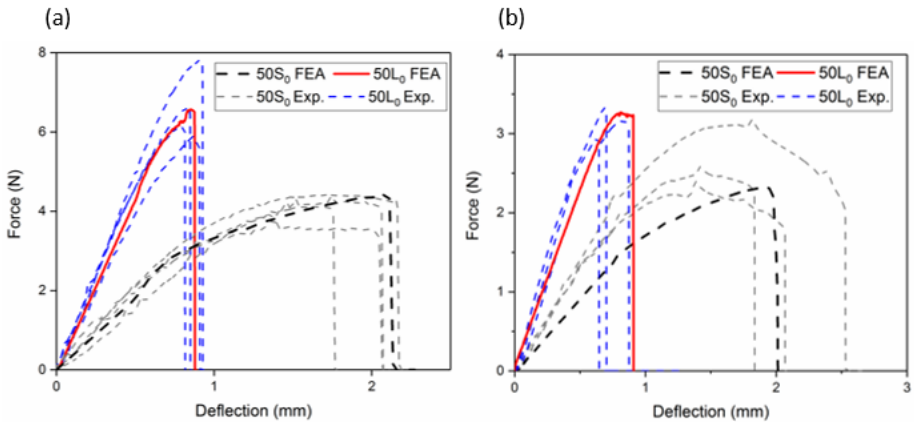

Figure 13 Inverse method and validation results for both *50S*$_0$ and *50L*$_0$ under (a) four-point bending and (b) three-point bending (Reprinted with permission from[35])

The silicone material properties were added into the full model for simulation (Fig. 10) after the brittle cracking model. The silicone phase was modeled with a hyperelastic material. The hyperelastic material setting with Marlow strain energy function was used, which was recommended by ABAQUS User's Guide [48] when only one set of test data is available. The uniaxial test data for silicone (Sylgard 184) were obtained from the literature [60, 61]. The Poisson's ratio of the silicone was set as 0.45 [62]. Figure 14 shows that the evaluation result of the hyperelastic model perfectly matches with the uniaxial engineering stress-strain data, verifying this automatically generated Marlow strain energy function. The full analysis was run with the explicit solver because of the requirement for the brittle cracking model. To save the computational time, the loading speed was set to be higher than the actual tests but remained in a quasi-static condition based on the rule that kinetic energy being less than 5% of the internal energy [63]. The viscoelastic property was not considered here due to a quasi-static bending study.

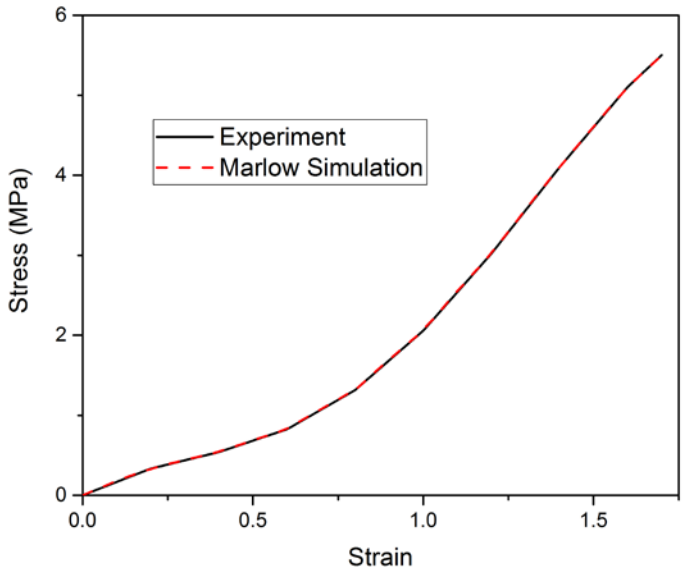

Figure 14 The fitting result of the hyperelastic model using Marlow strain energy function (Reprinted with permission from[35])

3.5. FEA and Experiment Comparisons

The numerical and three repeated experimental results of *type I* composite were shown in Fig. 15 (a) and (b) for *50S* and *50L*, respectively. Although the samples were fabricated following the identical procedures as described in Chapter 2, the experimental results still show noticeable variations due to the uncertainties of the printing nozzle, binder, and powder distribution as well as the inherent defects in the brittle frame. The maximum forces of *50S* are 7.2, 6.9, and 5.2 N; the stiffnesses are 7.2, 4.8, and 4.5 N/mm, respectively. For *50L*, the maximum forces are 12.4, 8.9, and 5.2 N; the stiffnesses are 15.2, 11.6, and 10.2 N/mm. Also, the first-drop points are at 0.82, 1.04, and 0.53 mm deflection, respectively.

Despite the variations, the overall behaviors are similar among experiments in each case and also similar to the FEA results. In *50S*, the force increases linearly at the beginning and transitions to a non-linear region at an almost identical point with the experimental results. FEA result also shows no structural damage in *50S*. The force profile starts to fluctuate at a higher deflection due to more significant element damages and deletion inside the structure. For *50L* FEA, there is a force drop occurs at 0.9 mm, which is within the range of the experimental data (0.5 to 1.1 mm). Another force drop is at 3.8 mm. Although the second structural damage can be seen in all three experimental samples, they occur at different deflection levels and not as apparent as in the model. In addition, the gradual loss of load carrying ability after 4 mm is not reflected by the FEA after the second force drop. This is due to no damage criteria for the silicone material, which is the limitation of hyperelasticity modeling [64].

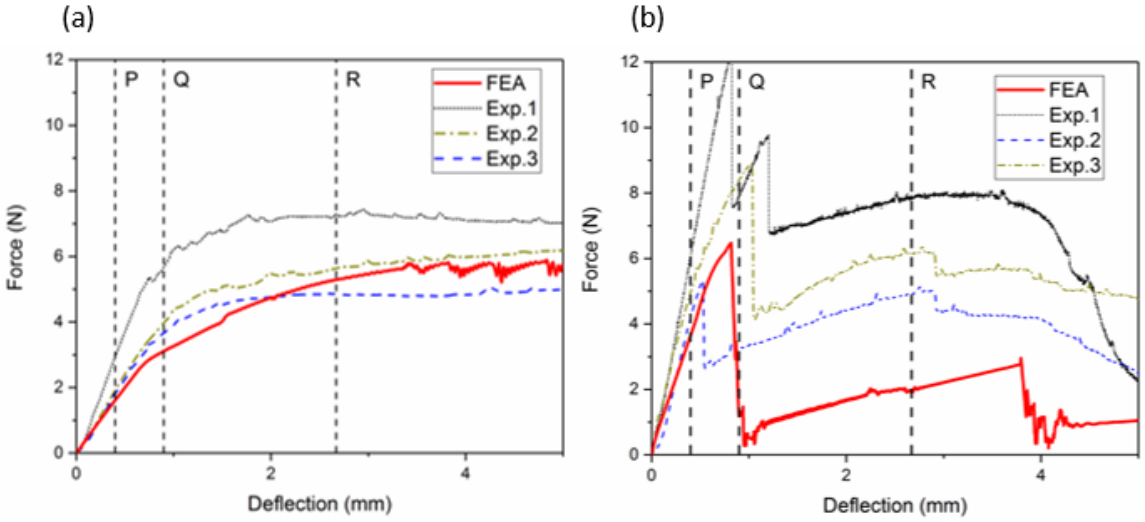

Figure 15 Experimental and FEA results of *type I* composite under four-point bending: (a) *50S* and (b) *50L* (Reprinted with permission from[35])

3.6. *Type I* Composite Damage Conditions

Finite element models can be used to explore the material degradation during the load carrying cycle. The FEA-simulated bending process at three deflection levels (marked by points P, Q, and R in Fig. 14) are shown in Fig. 16 for both *50L* and *50S*. The initial stiffness of *50L* is higher than that of *50S*. The *50L* has a higher overall stress level than that of *50S* at point P (Figs. 16 (a) and (b)) before the degradation takes place. At point Q, *50S* transitions into a non-linear region, and *50L* has a sudden structural damage. The structural damage of *50L* presents in Fig. 16 (c) that releases the stress from the structure, leading to a lower force level. In contrast, the symmetric stress distribution of *50S* in Fig. 16 (d) indicates none or little-damaged structure. The element degradation in the structure is not severe enough to trigger major crack damage. At point R with a large deflection level (2.7 mm), more damage can be seen in *50L*, such as missing elements and regional stress concentration. Also, asymmetric stress distribution in *50S* implies more degradation at the bottom of the beam where the material is subjected to tensile; however, there is no noticeable structural damage.

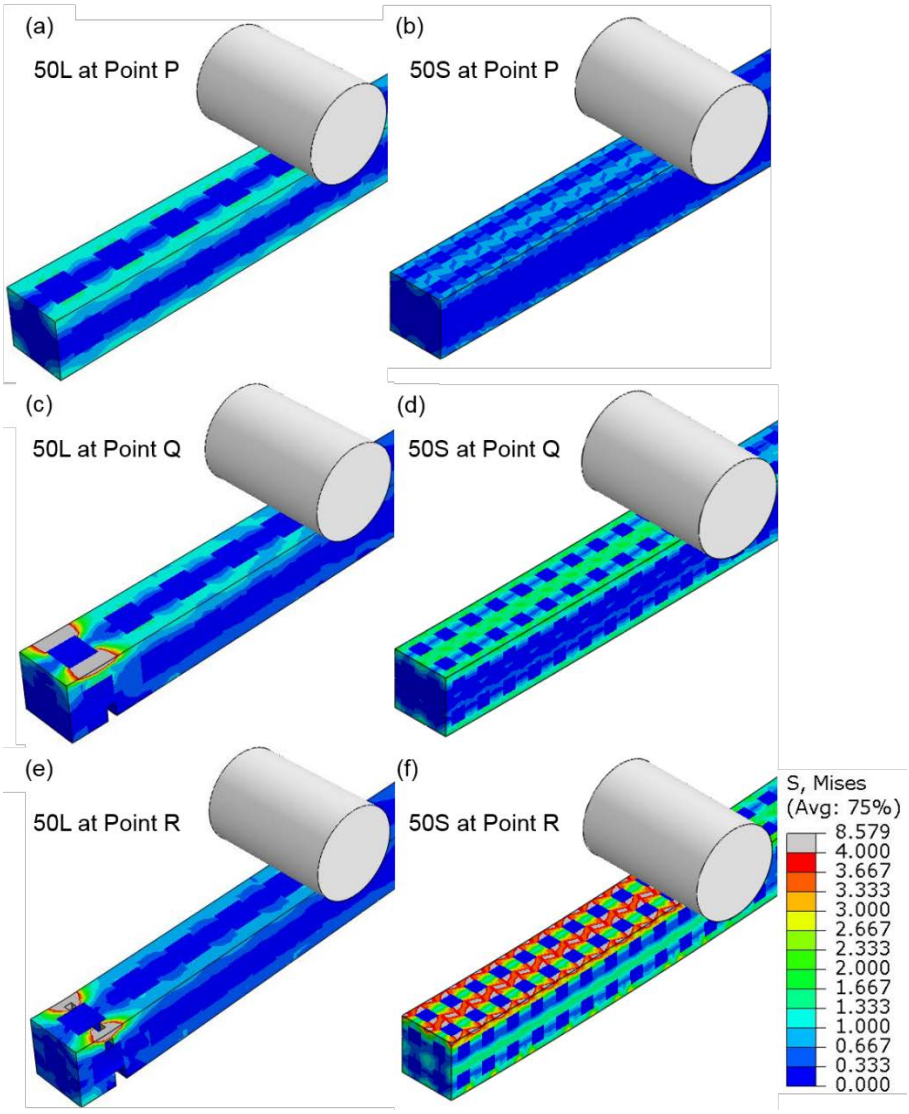

Figure 16 Visualization of FEA results for *type I* composite behaviors under four-point bending (Reprinted with permission from[35])

The silicone phase hinders the crack propagation and also provides a certain degree of strengthening effect due to the triaxial stress. Figure 17 shows the comparison of the bending behavior between a pure silicone elastomer structure and the silicone inside *type I* composite at the deflection level of 2.7 mm. The silicone in *type I* composite shows a

much higher stress than that of the pure silicone structure. This is due to the fact that silicone is constrained in the lattice structure; the high Poisson's ratio (0.45) leads to higher stress during deformation. The constraints from the surrounding brittle and stiff phase initiate the stress perpendicular to the stretching (tensile) direction, which forms a tri-axial stress condition. Therefore, although the silicone has minuscule strength compared to the plaster phase, the strengthening effect of silicone slightly increases the load carrying ability of the structure. This is evidence of the higher strength in *type I* composite compared to the pure plaster structure (Fig. 4).

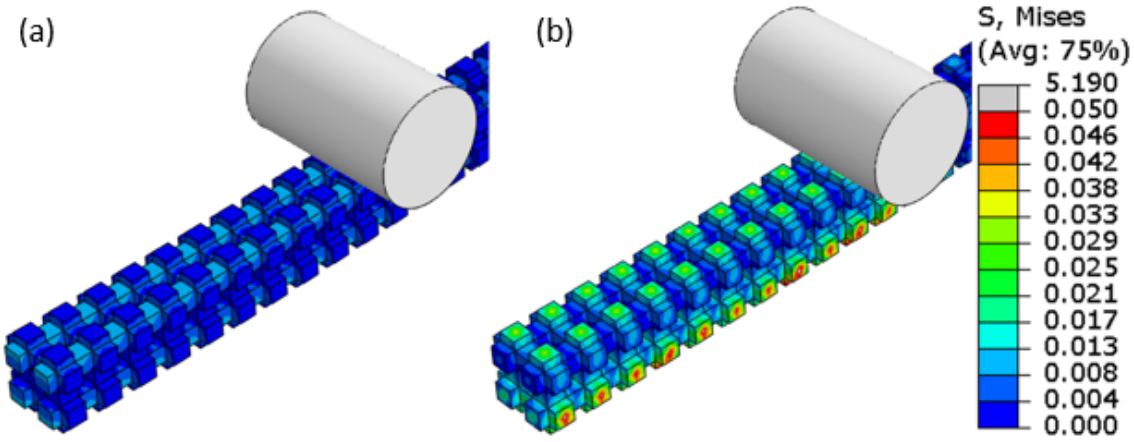

Figure 17 Simulated stress distributions of the silicone phase (a) without the constraint of the plaster structure (b) with the constraint of the plaster structure (Reprinted with permission from[35])

3.7. Model Limitations

Although the FEA model successfully explains the bending behaviors of *type I* composite, it is not yet a predictive model that can be used for performance prediction or

design optimization. In addition to the material variations from 3D printing, the following numerical limitations can possibly induce errors. First, the brittle cracking model does not incorporate compression damage. More complex loading conditions can lead to an inaccurate estimation from FEA. Second, the hyperelastic model has no failure definition. Under a large strain deformation, this can lead to a stronger and tougher structure than an actual one. Lastly, FEA is mesh-size dependent. Although the inverse-method-determined parameters (Sec. 3.4) have taken into account the mesh size effect, they may not be valid under excessive loadings or severe damage conditions.

3.8. Conclusions

This chapter discusses the bending behaviors of *type I* composite by using FEA method. The bending behaviors of *type I* composite were successfully modeled using an FEA method with the brittle cracking and hyperelastic material models. In comparison with other conventional FEA methods in crack modeling, this modeling method enabled the analysis with coarse and uniform mesh in the structure to represent the effect of microcracks inside the material. However, the model still has some limitations that require to improve further.

4. LOW-VELOCITY IMPACT BEHAVIORS OF TYPE II COMPOSITE – EXPERIMENTAL STUDY*

This chapter* presents a low-velocity impact response of *type II* composite by using the experimental method. T*ype II* composite is a structural composite consisting of a 3D-printed lattice structure made of polylactide (PLA) and filled with a polyurethane (PU) foam material for improving the impact resistance. Three different PU foams, including one rigid foam and two flexible foams, are selected to determine the foam reinforcement effect. The impact tests are conducted to compare the impact attenuation, ductility, toughness, and strength using the measured rate of change of acceleration (known as "jerk"), displacement, energy absorption, and the maximum acceleration, respectively. The results show that the flexible foams have more positive effects on the impact properties than the rigid foam. The maximum reduction of jerk is about 9% compared to the baseline structure without foam reinforcement. The maximum displacement is increased by 17%; the maximum energy absorption is increased by 23%. The maximum acceleration remains similar for all samples. In conclusion, the foam-filled *type II* composite can retain a similar strength while enhancing the ductility and energy absorption.

---

* Reprinted with permission from "Low-velocity impact response of 3D-printed lattice structure with foam reinforcement." Kao, Y. T., Amin, A. R., Payne, N., Wang, J., & Tai, B. L., 2018, *Composite Structures*, *192*, 93-100. Copyright 2018 by Elsevier B.V.

4.1. Introduction

An ideal impact-resistive composite requires the abilities to attenuate impact and absorb the kinetic energy effectively. These materials can be used in applications such as helmets and portable electronics [65-68]. Conventionally, engineers adopt a sandwich structure composed of two rigid plates and a cushioning material or cellular structure in the middle to dampen the impact [69-72]. This is known as a structural composite. Zhang et al. [18] presented a different idea of the structural composite using a polyurethane-foam-filled pyramidal lattice. The results showed that the specimen with foam-filled core had a significant improvement of energy absorption in compression tests compared to those with an unfilled core, but the improvement of impact properties was little. Although this kind of structural composite shows preferable mechanical properties, this pyramidal lattice core sandwich panel requires complex manufacturing methods, such as slot-fitting and an adhesive method [21, 22, 73], extrusion and electrical discharge machining [23], or a perforating technique [24, 25].

With the emergence of additive manufacturing technologies, the manufacturing processes of complex structural composite has become more accessible, even with more material options. 3D printing-built structural composite was demonstrated in the previous chapters. A binder-jetting printer was used to build a brittle and hard lattice frame, and the frame was impregnated with a silicone elastomer to enhance the toughness. The elastomer slowed down crack propagation in the frame structure, thus preventing a rapid brittle fracture. The mechanical properties could be significantly altered by the composition ratio of materials and the frame structure.

This chapter focuses on the impact behaviors of *type II* composite when a cushioning material is used as the reinforcement. The frame structure is made of polylactide (PLA) because of its wide accessibility and reasonable strength and ductility. Polyurethane (PU) foams are selected because of the cushioning characteristics. Foams are also light in weight and can create a strong bonding with PLA to avoid material de-cohesion. The drop-weight test is adopted to evaluate the impact responses of *type II* composite.

4.2. Materials and Methods

4.2.1. *Type II* composite Materials and Specimen Preparation

Type II composite is a lattice structure composed of a 3D-printed PLA frame impregnated with foam. A fused deposition modeling (FDM) 3D printer, Dreamer (Flashforge, Zhejiang, China), is used to create the PLA frame. The *type II* composite design, as shown in Fig. 18 (a), is based on a 6.5 mm unit cube to form a beam structure with dimensions of 13 mm by 13 mm by 149.5 mm. The length and width are following the ASTM D7264 [36] standard for three-point bending test, and the thickness is designed to fit two complete unit cells. The void-to-solid ratio of each unit cell determines the volume fraction of the foam in a *type II* composite. This volume fraction is set to be 50% as a control variable in the experiment. After printing, the foam is added to the frame by a molding process, which refers to “impregnation.” The mold consists of two pieces, as shown in Fig. 18 (b), with the top one having through-slots to fit *type II* composite samples. The plates are clamped together to avoid movement during the curing process. This mold design allows an easier post-process to remove the excess foam on the top surface and to

demold the cured sample. Fig. 19 shows the manufactured *type II* composite samples with three different foams.

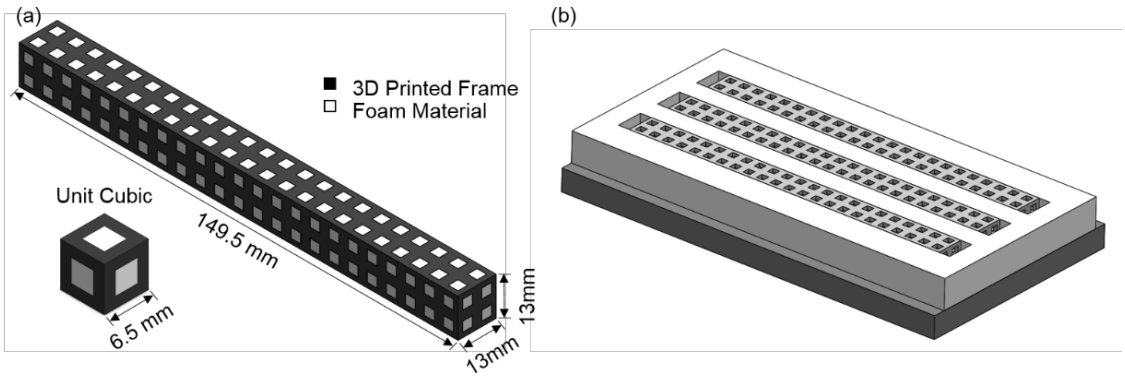

Figure 18 *Type II* composite fabrication: (a) the unit-cell design and (b) the molding method (Reprinted with permission from[74])

Figure 19 Manufactured *type II* composite samples with three different types of PU foams (Reprinted with permission from[74])

Three foams are selected from Smooth-on Inc. (Macungie, PA) to reinforce the lattice structure. Foam-it 8 (denoted as *FI-8*) is relatively light, porous, but is more brittle. FlexFoam-it 17 (*FF-17*) and FlexFoam-it 25 (*FF-25*) are both flexible foams but much denser than FI-8. To quantitatively determine their individual mechanical properties, they are made to a dog-bone shape, as shown in Fig. 20, for a uniaxial tension test following ASTM D3574. Table 2 lists the tensile testing results, including a printed PLA. *FI-8* has the elastic modulus ten times lower than that of PLA, but higher than those of *FF-17* and *FF-25* by a magnitude of two. FI-8 has an extremely low tensile strength and toughness among all. *FF-17* and *FF-25* have higher toughness than that of PLA, and *FF-17* is the toughest.

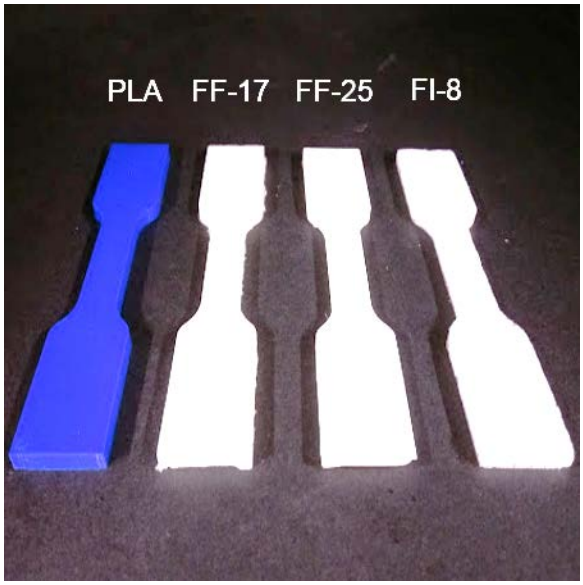

Figure 20 Manufactured tensile test samples (Reprinted with permission from[74])

Table 2 Mechanical properties of the materials determined by the uniaxial tension (Reprinted with permission from[74])

	Elastic Modulus (MPa)	*Max Stress (MPa)*	*Max Strain*	*Toughness (J/m^3)*	*Density (g/cm^3)*
PLA	1358.10	29.39	0.030	551200	1.27
FI-8	140.15	0.45	0.003	700	0.13
FF-17	1.54	1.67	1.054	851700	0.27
FF-25	1.52	1.33	0.824	596100	0.40

4.2.2. Experimental Setup and Design

Figure 21 shows the setup of the low-velocity drop weight test used in this study. The low-velocity impact typically has an impact velocity less than 10 m/s for the target applications such as helmets and portable electronics. The three-point bending configuration follows the ASTM D7264 [36]. An integrated electronic piezoelectric triaxial accelerometer (Type 8766A, Kistler, Switzerland) is used for measuring the acceleration because of its high-sampling rate compared to the conventional capacitor-based accelerometers. The signal is captured through an amplifier (Type 5165A4, Kistler, Switzerland) and a data acquisition system at the highest sampling rate 62,500 Hz of the accelerometer.

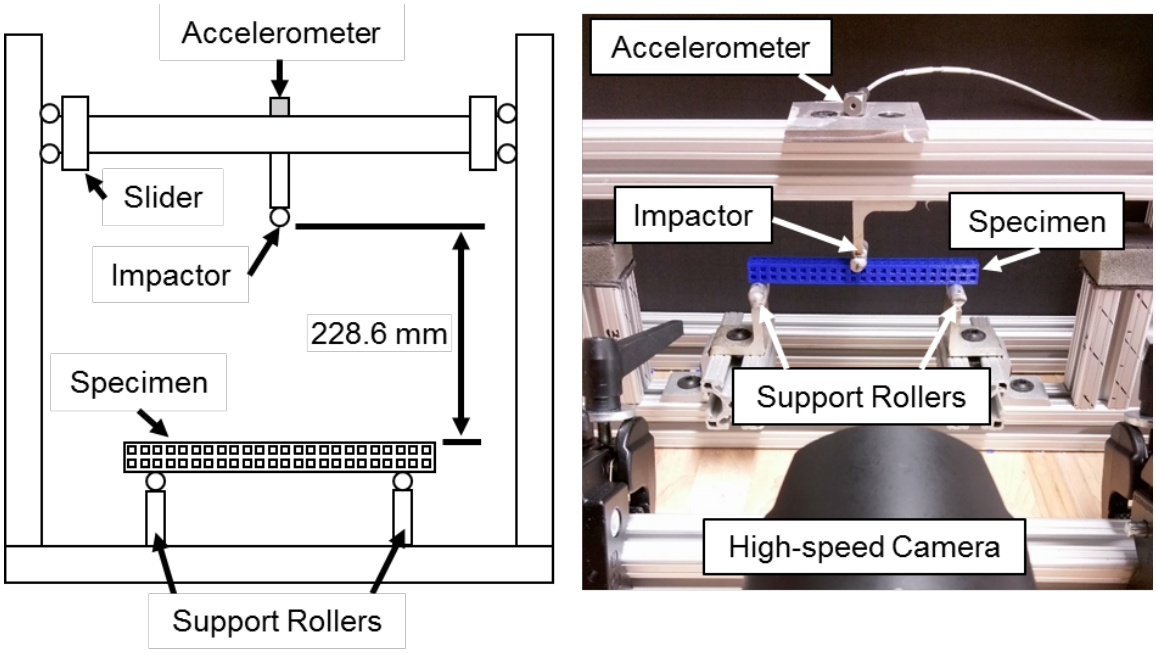

Figure 21 Design and actual setup of the drop-weight impact test (Reprinted with permission from[74])

Typically, a drop test can be designed to measure the energy absorption by breaking the sample or stopping the impactor on the sample to determine the impact attenuation. Provided the high-sampling-rate capability, it is possible to obtain both the energy absorption and attenuation in a destructive drop test. Therefore, in this study, all specimens are tested at a drop height of 228.6 mm (9 in), which has been tested to be sufficient to break all the samples. The impact velocity is about 2.12 m/s without considering air drag force and friction on the drop system. A high-speed camera (Phantom Miro Lab310, Vision Research, Wayne, NJ) is used to capture the point of contact, crack initiation, and sample failure at a frame rate of 35,000 per second. The images are used to cross-compare the acceleration data and to examine the fracture phenomenon during the impact. The

frame rate, shutter time, and light setting are selected to obtain valid experimental outcomes.

In the experiments, *type II* composite samples with three different foams are compared to a pure type II frame with no impregnation as the baseline. A total of 15 samples are tested for each *type II* composite to minimize the experimental uncertainties and variations. Four impact properties are extracted from the acceleration data, including the maximum acceleration, the rate of change of acceleration (known as "jerk"), energy absorption, and the maximum displacement. The data processing methods are detailed in the next section.

4.2.3. Data Processing and Analysis

A typical example of the filtered acceleration data obtained from the data acquisition system is shown in Fig. 22 (a) (the *a-t* curve). The impact region considered in this study is from Point A to Point C. Point A corresponds to the impact starting point, which is the moment when the impactor contacts the specimen. Point B is the maximum acceleration during the test, which is also the maximum force acting on the structure. Jerk (m/s^3) can be calculated from a linear regression from Point A to Point B. Point C is the specimen failure, which occurs almost immediately after Point B. The duration of the impact is around 0.0034 s in this particular example.

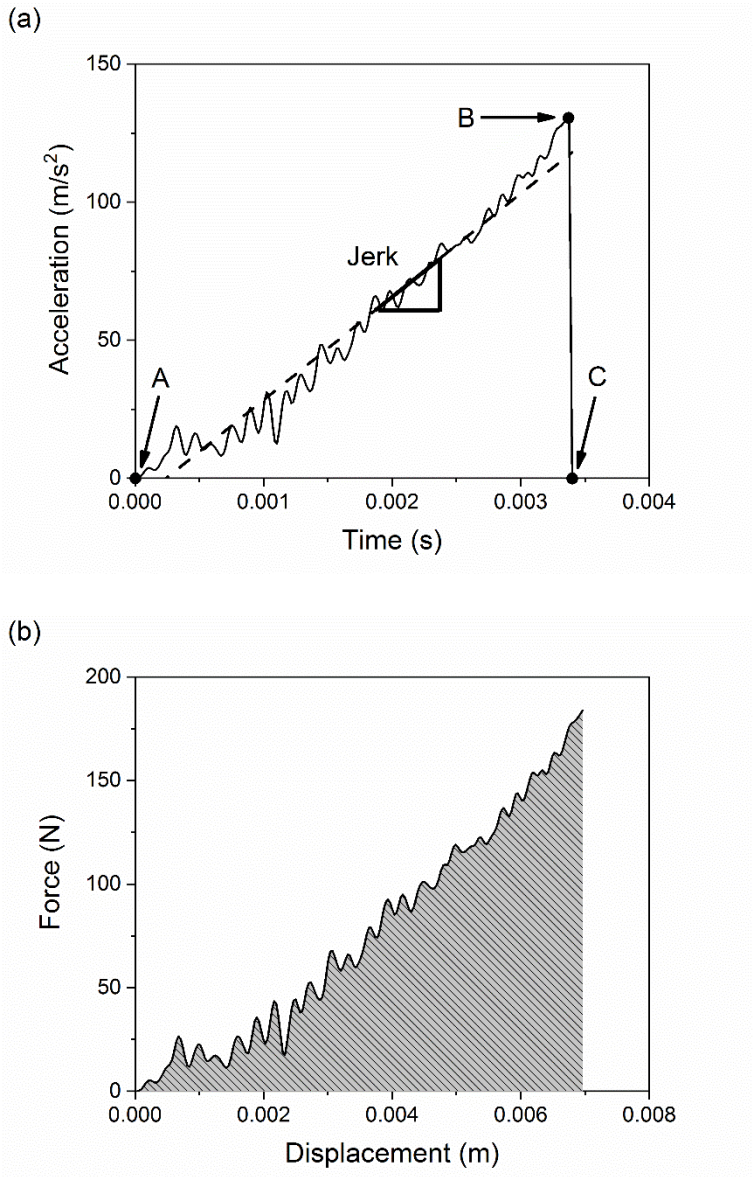

Figure 22 An example of data processing: (a) acceleration-time curve and (b) force-displacement curve (Reprinted with permission from[74])

To find the energy absorption, the acceleration-time curve is converted to a force-displacement curve by the following four steps. The first step calculates the initial velocity

(V_0) of the impactor at the impact starting point (Point A) by Eq. (1) assuming a free-fall condition.

$$V_0 = \sqrt{2gh} \tag{1}$$

The initial velocity is 2.12 m/s given the height h of 228.6 mm (9 in) and g = 9.81 m/s^2. Second, the velocity V at an instantaneous time t_x can be calculated by

$$V(t_x) = V_0 - \int_0^{t_x} a(t)\, dt \tag{2}$$

where $a(t)$ is the time-series data of acceleration of the impactor. The negative sign means that the acceleration is in the opposite direction to the velocity. The time t_x is based on the beginning of the impact. The third step finds the displacement d at a given time t_x using Eq. (3).

$$d(t_x) = \int_0^{t_x} V(t)\, dt \tag{3}$$

Lastly, the impact force F conversion is using Newton's second law, such that

$$F(t_x) = ma(t_x) \tag{4}$$

where m is the mass of the impactor carrier, including the impactor, sliders, aluminum bar, and the accelerometer. In this study, the total mass of the impact system is around 1.4 kg. The converted force-displacement (*F*-*d*) curve of Fig. 22 (a) is shown in Fig. 22 (b). The *a*-*t* and *F*-*d* curves are similar here because the velocity drop during this impact is small (~15%), the displacement change is almost linear with time. The maximum displacement is the point at which the force drops to zero. To be noted that this displacement is not necessarily equal to the beam deflection since the impact may cause local deformation on the structure.

For each drop test, the impact properties, including jerk, maximum acceleration, energy absorption, and the maximum displacement, can be extracted from *a-t* and *F-d* curves. A total of 15 tests are repeated for each sample, including the baseline pure type II frame. The Dunnett's test [75] is used for statistical comparison since it is more rigorous than *t*-test when comparing any two independent variables in a multiple comparison procedure. The analysis is tested at the 95% significance level (i.e., p-value = 0.05). The error bar corresponds to one standard error.

4.3. Experimental Results

The impact properties are compared in this section. The jerk represents the ability to attenuate an impact shock. The maximum displacement is the combination of local deformation and global deflection, which are related to the modulus of elasticity and bending stiffness, respectively, during an impact. Energy absorption defines the impact toughness. The maximum acceleration represents the maximum force carried by the structure, meaning the material strength.

4.3.1. Results of Impact Properties

Fig. 23 shows the maximum displacement of the impactor for each *type II* composite. Flexible foams, *FF-17* and *FF-25*, increase the maximum displacement by 17% and 16%, respectively, compared to the baseline pure *type II* frame. This result indicates that flexible foams, when having sufficient ductility, can reduce the impact shock and thus allow more strain in the *PLA* frame. On the contrary, the rigid foam *FI-8* reduces the level of maximum displacement about 5%, although the difference is not statistically significant. The

tendency to reduce the maximum displacement is due to the high stiffness and low ductility of *FI-8* that decrease the overall structural flexibility.

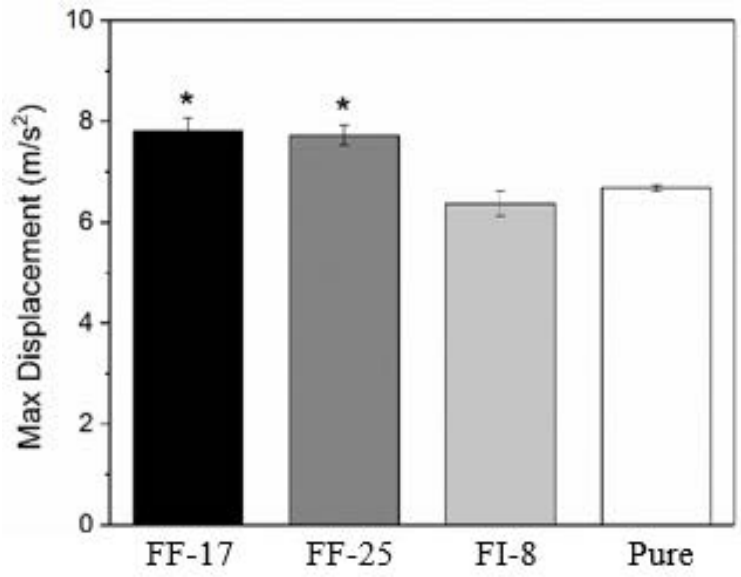

Figure 23 Maximum displacement of *type II* composite samples. * represents a statistical significance ($p < 0.05$) compared to pure *type II* frame. (Reprinted with permission from[74])

The results of energy absorption for *type II* composite samples are shown in Fig. 24. The flexible foam *FF-17* increases the energy absorption by 23%, which is the highest among the three foam materials and the only one having a statistically significant difference from pure *type II* frame. This is likely because of that *FF-17* has the highest toughness and strength among the three foams. Although not as much, *FF-25* also increases energy absorption by 17%. This can be explained by that the toughness of *FF-25* is slightly lower than that of *FF-17*. Opposed to the flexible foams, the rigid foam *FI-8* decreases the energy absorption by 3%.

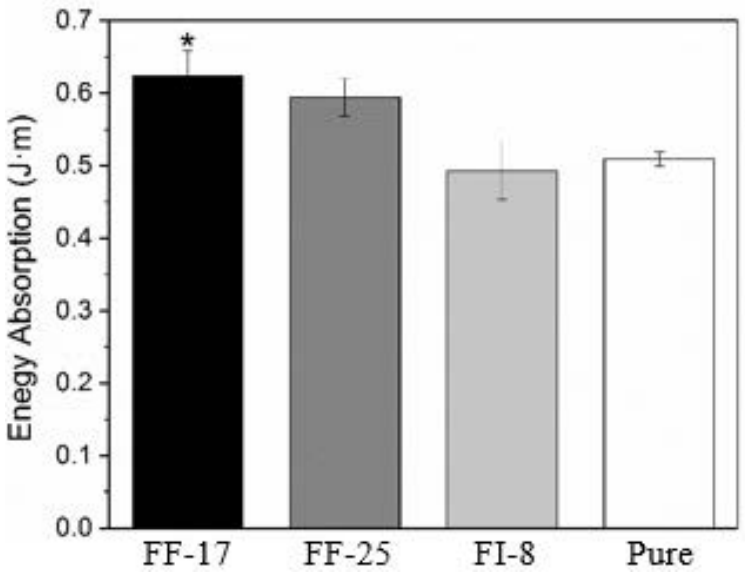

Figure 24 Energy absorption of *type II* composite samples. * represents a statistical significance ($p < 0.05$) compared to pure *type II* frame. (Reprinted with permission from[74])

Fig. 25 shows the results of the maximum acceleration of each *type II* composite. Generally, adding another foam material can increase the maximum acceleration because the material becomes stronger. However, according to the results, the increase is negligible and not statistically significant. This indicates that the PLA frame till dominated the strength of *type II* composite, and the foams do not make as a significant effect on the strength.

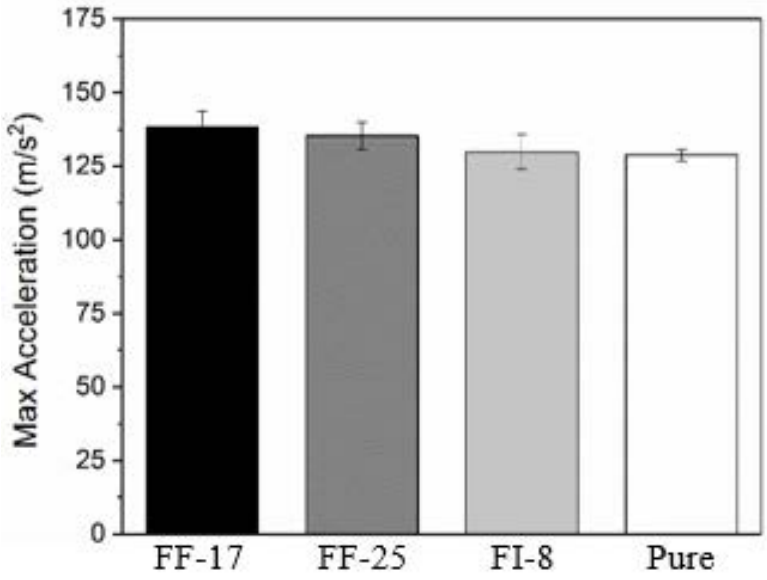

Figure 25 Maximum acceleration of *type II* composite samples. * represents a statistical significance ($p < 0.05$) compared to pure *type II* frame. (Reprinted with permission from[74])

The results of the jerk for *type II* composites are shown in Fig. 26. The results indicate that impregnating a foam into a pure *type II* frame significantly changes the ability to attenuate impact. The flexible foams, *FF-17* and *FF-25*, reduce the jerk about 9% with statistical significance (p-value < 0.05), but the difference between the two materials is negligible. However, the rigid foam (*FI-8*) has the opposite effect. It increases the jerk by 7% compared to that of pure *type II* frame.

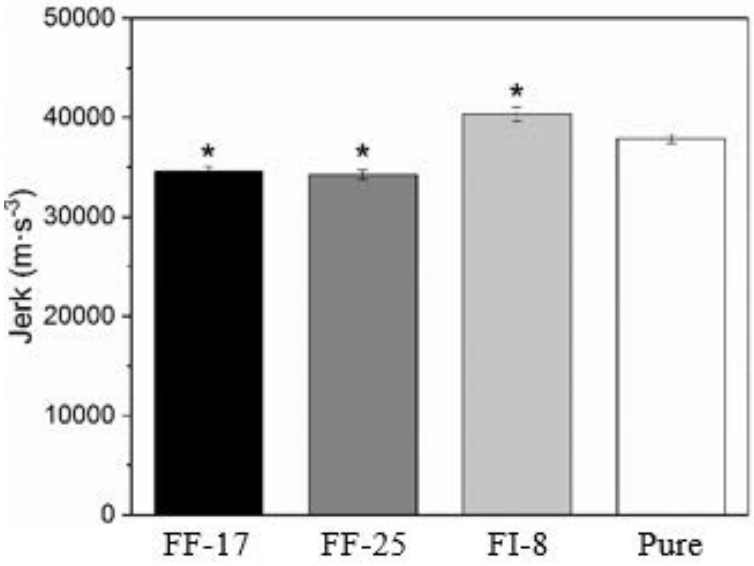

Figure 26 Jerk of *type II* composite samples. * represents a statistical significance ($p < 0.05$) compared to pure *type II* frame. (Reprinted with permission from[74])

4.3.2. Results from High-speed Images

Multiple images are extracted from the high-speed camera to compare the impact behaviors at three instantaneous moments: the contact point between the impactor and the specimen, the point when the first crack is observed, and the point of a complete failure. These images are sorted in Fig. 27. With flexible foams (*FF-17* and *FF-25*), the crack propagates steadily from the bottom of the structure towards the top surface. However, with the rigid foam *FI-8*, the crack initiates and propagates without any particular direction. This phenomenon is also seen in pure *type II* frame. In addition, *FI-8* is so brittle that can initiate multiple cracks at impact. *FF-17* and *FF-25* are relatively ductile and tough, so they require a higher stress concentration to open a crack.

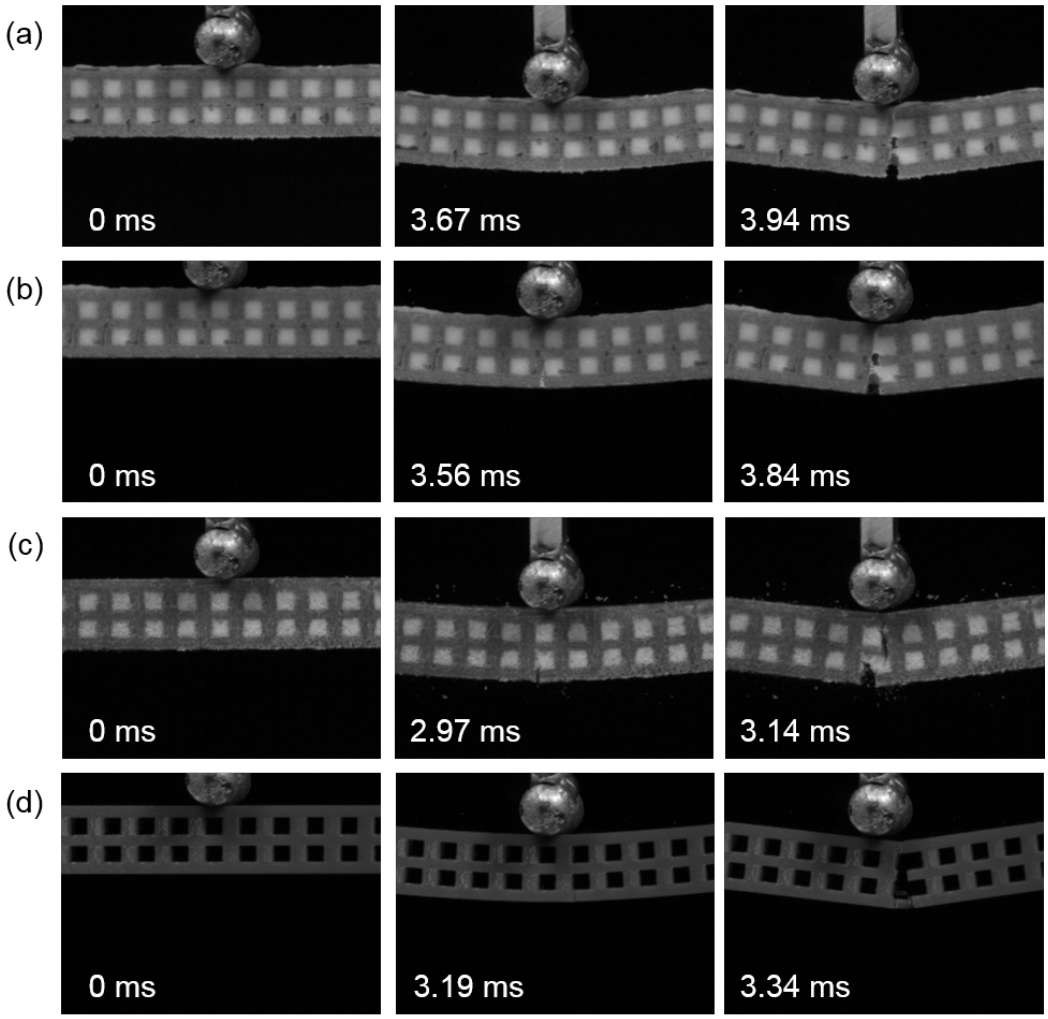

Figure 27 High-speed images at different instantaneous times during impact for *type II* composite *with* (a) *FF-17* (b) *FF-25* (c) *FI-8* and (d) pure *type II* frame (Reprinted with permission from[74])

Fig. 28 shows the side-by-side comparisons of impact time duration among these cases. The flexible foams, *FF-17* and *FF-25*, significantly increase the durations of contact to crack initiation and crack initiation to failure. Because of the cushioning effect of these flexible foams, it takes a longer time to reach the maximum strength of PLA prior to rupture. For the time duration from crack initiation to failure (i.e., post-failure region), the

flexible foams act as an impediment to prevent the cracks from propagating rapidly through the structure. Although the rigid foam *FI-8* makes the specimen behaves differently compared to the pure type II frame, the difference is negligible. This is because *FI-8* fails at a lower strain level than PLA.

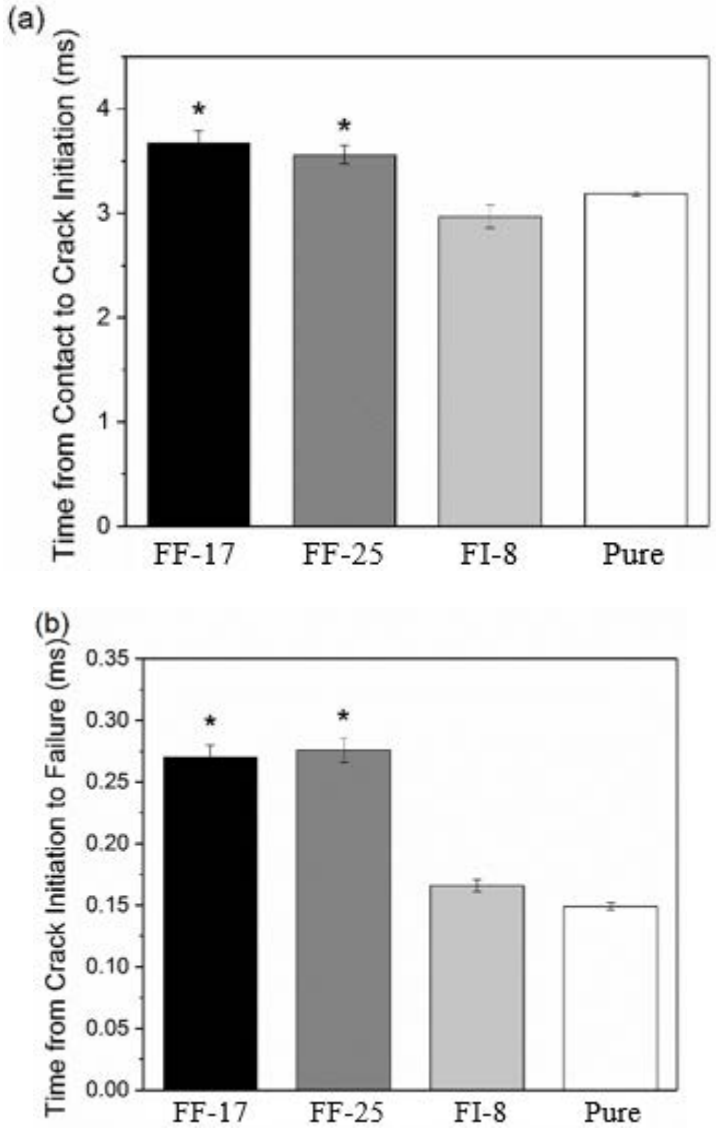

Figure 28 Time duration of impact (a) from contact to crack initiation (b) from crack initiation to failure. * represents a statistical significance ($p < 0.05$) compared to pure *type II* frame. (Reprinted with permission from[74])

The high-speed images were also used to verify the accuracy of the filtered a-t curves from the accelerometer. The total time duration of impact from the high-speed camera is less than 2 % different from the time in the a-t curves (Point A to C in Fig. 22(a)).

4.4. Discussion

4.4.1. Material selection criteria

The impact properties measured in this study include jerk, maximum acceleration, maximum displacement, and energy absorption. These properties are found highly dependent on the mechanical properties of the foam. Based on the experimental results, a general guideline for selecting a proper foam is concluded below.

For the applications that require a low jerk response, the material must have a much lower elastic modulus than that of the frame. This approach avoids increasing the overall stiffness of *type II* composite, which is proportional to the impact shock. Both flexible foams in this study (*FF-25* and *FF-17*) have an elastic modulus about 100 times lower than that of PLA. Therefore, they can decrease the jerk.

A flexible and viscoelastic foam also protects the PLA frame from immediate impact fracture by slowing down the stress wave and abrupt crack propagation. The foam must have a much higher ductility than PLA to tolerate excessive local deformation. In this study, *FF-17*'s fracture strain is 35 times higher, and *FF-25*'s is 27 times higher than that of PLA. For the same reason, the rigid foam (*FI-8*) does not increase the maximum displacement due to its brittleness. Consequently, the additional energy absorption by the brittle foam is minimum.

The maximum acceleration represents the maximum force taken by the structure prior to fracture, so it also represents the structural strength under impact. There is no statistical difference among these tested *type II* composite samples because the foams are much weaker than PLA (about 5% of the PLA's strength). The PLA frame carries the major load. However, a slight increase can be seen with *FF-17* and *FF-25* due to their ability to allow more deformation on the PLA frame as previously mentioned.

Lastly, it should be mentioned that a strong bonding strength between foam and frame material is necessary to maximize a *type II* composite's impact properties. A strong bonding allows the cushioning material to carry the stress wave from the impact effectively. In a past study, Amin et al. [76] showed that impregnating a silicone viscoelastic material as the cushion does not have any influence on the impact behaviors because of its weak bonding between the silicone and the PLA. In comparison, PU foam-PLA bonding is sufficient. Although there are a few local interfacial failures near the cracking path, no noticeable de-cohesion is found.

4.4.2. Necessity of structural design

Although this chapter focuses on the material effects on the impact properties, it should be noted that the structural design plays a significant role in the material performance of the *type II* composite. When the foam is flexible, the frame structure dominates the bending stiffness by its elastic modulus and the moment of inertia. The structural change will also affect impact properties via various mechanisms. To further demonstrate the potential of *type II* composite, this section presents a simple test that compares the solid PLA structure and a conventional sandwich structure using the same foam material (*FF-*

17) and composition ratio (50%). These samples are shown in Fig. 29, followed by the impact testing results in Fig. 30.

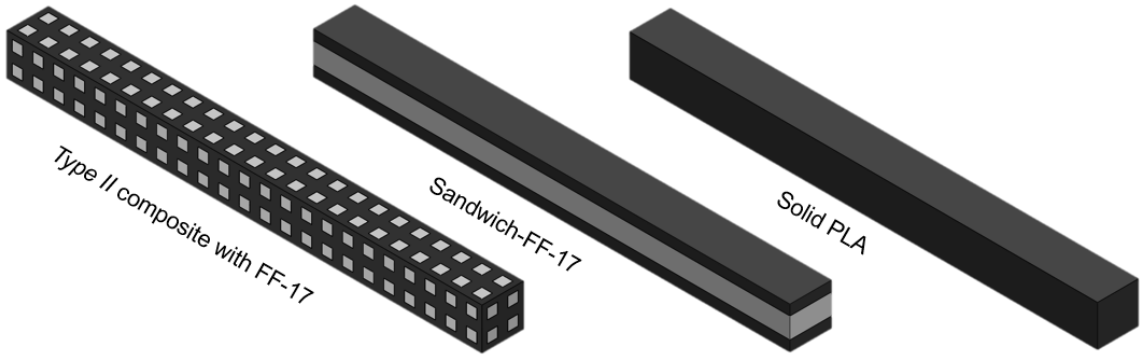

Figure 29 Samples of *type II* composite with FF-17, sandwich structure, and solid PLA bar (Reprinted with permission from[74])

Undoubtedly, the solid PLA bar has the highest acceleration and the highest jerk because of its high stiffness. The impact shock could be substantial on the solid PLA. On the other hand, the sandwich structure with 50% foam material has the lowest acceleration and jerk, indicating a significant damping effect. It also has the largest amount of energy absorption due to a much higher local deformation on the top of the sample. However, as a trade-off, the sandwich structure has the weakest structural strength and stiffness. Also, the properties of the sandwich structure are anisotropic; its performance depends on the direction of impact. If the sample is rotated axially by 90˚, all impact properties will change as the foam does not increase any local deformation on the top of the specimen in this scenario.

In comparison, *type II* composite offers a compromise to balance between the structural strength, stiffness and the impact attenuation. Also, *type II* composite is generally isotropic. The viscoelastic properties of the foam could possibly improve energy absorption.

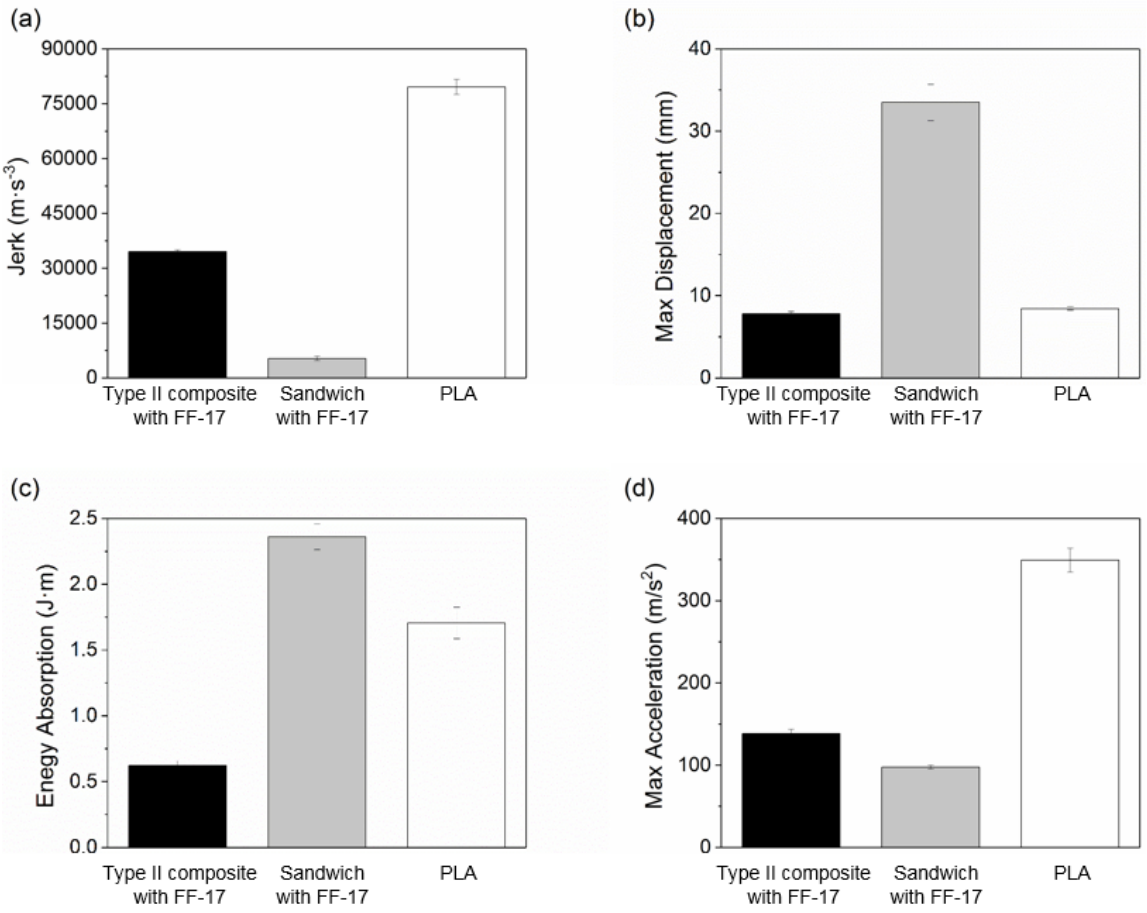

Figure 30 Comparisons of impact results among *type II* composite, sandwich structure, and solid PLA: (a) Jerk (b) Maximum displacement (c) Energy absorption and (d) Maximum acceleration (Reprinted with permission from[74])

The application and needs drive the structural design of the *type II* composite. Although not particularly discussed, the optimization will require the cooperation of both

cushioning material and frame structure because of their coupled effects on mechanical behaviors.

4.5. Conclusion

This chapter presents the effects of material selection on the impact properties of the *type II* composite. Three different foams are selected with a 3D-printed PLA lattice frame. The experimental results show that different foams affect the impact properties differently and do not always show improvement. The main findings are summarized as follows. First, to reduce the impact shock, the foam must have a low elastic modulus not to change the overall structural stiffness. The viscoelasticity of the foam can aid more energy dissipation and stabilize crack initiation and propagation. Second, to improve the energy absorption, the foam must have a high ductility to allow excessive local and global deformation upon impact.

5. LOW-VELOCITY IMPACT BEHAVIORS OF TYPE II COMPOSITE – NUMERICAL STUDY

This chapter presents a finite element analysis (FEA) on low-velocity impact response of a foam-filled lattice composite. The composite consists of a 3D printed polylactide (PLA) lattice frame and a polyurethane (PU) foam cast into the lattice space. A prior experimental study showed that the PU foam could increase the overall structural ductility and energy absorption during an impact at 2.12 m/s. To explain these phenomena, the FEA adopts an elastic material model for the PLA frame and a viscoelastic model for the PU foam to simulate the impact process. The results show that, although the foam does not significantly increase the stiffness and strength of the composite, it can redistribute the stress on the PLA frame, thereby enhancing the structural ductility.

5.1. Introduction

Additive manufacturing (also known as 3D printing) can create complex structures, reduce material waste, and accelerate manufacturing under low-volume production. Recently, using additive technologies to manufacture composite materials has drawn a lot of attention [77-82]. Composite materials are preferable in many engineering applications because of the high specific strength, excellent corrosion properties, and improved fatigue properties. 3D-printed composite research has been focused on particle reinforced composite materials [30, 83, 84] and fiber-reinforced composite [85, 86]. Some studies also used 3D printing for structural composites, such as sandwich structure [87, 88], honeycomb composite [89, 90], cellular structure [91], and lattice structure [35, 37, 74].

In the previous chapter, a structural composite composed of a 3D printed polylactide (PLA) lattice structure and a polyurethane (PU) foam filling was introduced for enhanced impact properties by taking the advantages of the compliance of the lattice structure and cushioning of the foam. The results under a low-velocity impact (2.12 m/s) showed that after the foam addition, the structural deflection could increase by 17%, the energy absorption can increase by 23%, and the jerk (the rate change of acceleration) can reduce slightly by 9% before structure failure. Although the study has successfully demonstrated the positive effects of foam filling, the reinforcement mechanism is still not well understood because, unlike other composite materials having a strong second phase for reinforcement, the PU foam is significantly softer than the PLA frame. Therefore, the objective of this study is to find the underlying mechanism for the enhanced impact performance.

Finite element analysis (FEA) is adopted in this chapter as it has been used to analyze 3D printed structural composites [92, 93]. L. Wang et al. [94] investigated the macroscopic mechanical properties of a 3D printed periodic glass polymer/elastomer co-continuous composite by using representative volume elements with FEA. The elastic-viscoplastic material model was used on the glassy polymer, and the hyperelastic material model was used on the elastomer. The uniaxial compression results showed that the mutual constraints between two phases of the composite lead to multiple cracks. M.R. Mansouri et al. [95] used experimental and finite element methods to analyze a fused deposition modeling (FDM) made the co-continuous composite. The FEA included two different hyperelastic material models. The compression results showed that the second phase in

the composite hindered the shear band development, so that the composite can undergo a higher strain without failure. Despite successful FEA, these works were all under a quasi-static condition, while the structural behavior can be more complicated under a dynamic event like impact. For example, structural vibration can lead to large stress concentration; materials are strain-rate dependent.

In this chapter, the type II composite is modeled with two sections. The first section, PLA lattice frame, is modeled as an elastic material with its properties determined using an inverse method to account for the printing quality. The second section, PU foam, is modeled as a viscoelastic material using Prony series with the coefficients determined by relaxation tests. Several assumptions are made in this work to increase the model efficiency, including model isotropy, constant Poisson's ratio, and no interfacial detachment, which will be justified in a later section.

5.2. Model setup and parameters

This section presents the setup and parameters of the FEA model. The model was constructed using ABAQUS (version 6.14-2) to simulate the low-velocity impact behavior.

5.2.1. Model geometry and boundary conditions

In the experiment, the lattice composite was created with a 3D printed PLA frame and filled with a PU foam (FlexFoam-iT 17, Smooth-on Inc.), as shown in Fig. 31(a). The dimensions were 13 mm by 13 mm by 149.5 mm. The composite samples were subject to a low-velocity impact test following the ASTM D7264 [36] shown in Fig. 31(b). The

diameters of the impactor and support pins were all 10 mm. The drop height was 228.6 mm (9 in), and the initial impact velocity was 2.12 m/s. With a total mass of 1.4 kg, the momentum at impact was calculated to be 2.97 kgm/s.

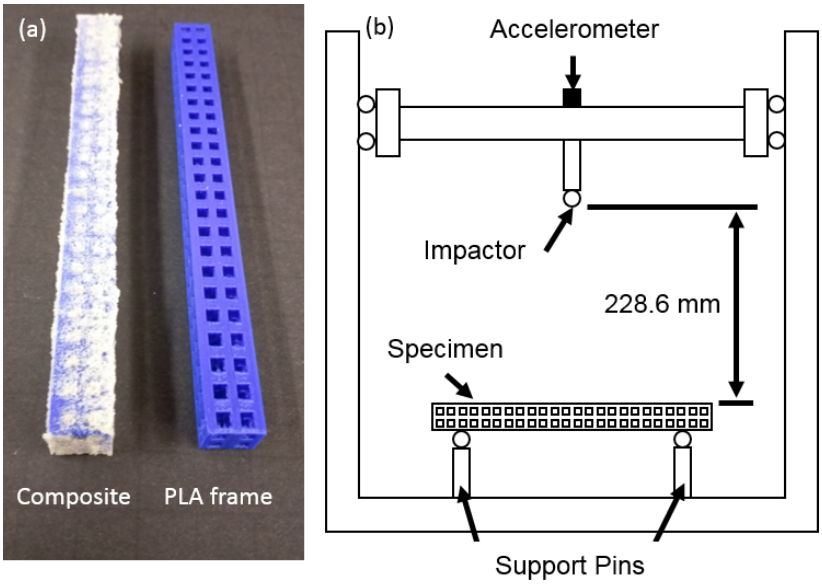

Figure 31 (a) 3D printed PLA frame and composite (b) the drop-weight impact test setup

The corresponding FEA model is created (Fig. 32), which consists of PLA frame and PU-foam. The elements with white and green colors represented the PLA frame, and the red elements were the PU foam. A cubic brick element (C3D8I) with 0.40625 mm unit length was chosen throughout the model to ensure the compatibility across the two materials. A perfect bonding was assumed between the PLA and foam material based on the experimental observation that no delamination occurred prior to structural fracture. A small value of friction coefficient between the specimen and the pins was defined to avoid

numerical instability, for which $\mu = 0.05$ was used [96, 97]. The top and bottom pins were both rigid bodies. The EXPLICIT solver was used to solve this problem in two steps: In Step 1, an initial velocity of 2.12 m/s and a 1.4 kg weight were assigned to the top pin to provide the momentum correspondent to the experiment at the initial contact. In Step 2, the gravitational acceleration, 9.81 m/s2, was applied to the whole model to simulate a free-fall condition during impact. The movement of the bottom pins was fixed in both steps, and that of the top pin is limited to the gravity direction (Y-axis) only.

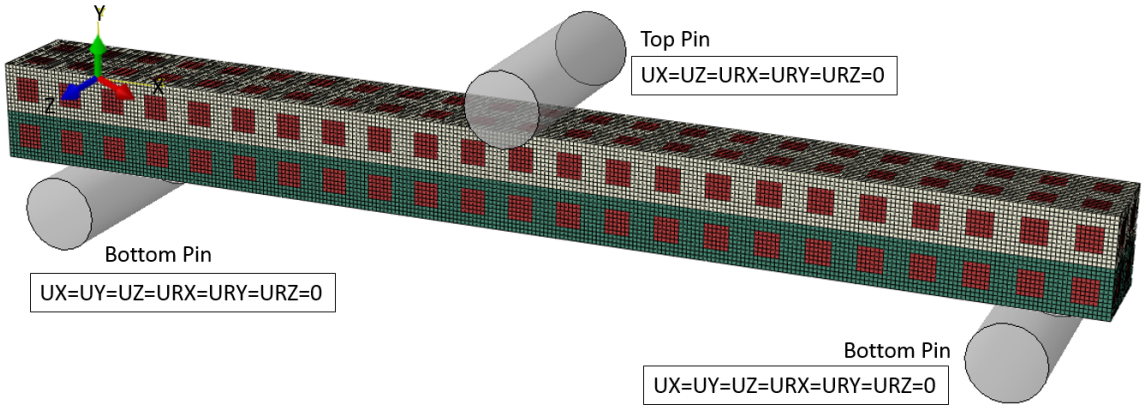

Figure 32 FEA model configuration for *type II* composite

5.2.2. 3D printed PLA lattice structure

3D-printed PLA is known to have different mechanical properties from those of the bulk form, and these properties are often anisotropic and strain-rate dependent. Therefore, an inverse method was used to experimentally determine an equivalent modulus of elasticity and strength of the printed PLA structure using an identical three-point bending configuration.

To estimate the PLA's properties under a high strain rate, the three-point bending test results under various bending speeds are shown in Fig. 33, which were obtained using a United Universal Testing Machine following ASTM D7264 [36]. The selected speeds of the crosshead pin were 1.27 mm/min, 127 mm/min, 508 mm/min, and 1270 mm/min (the highest possible speed). As shown, the loading rate had a small effect on the elastic modulus, but it significantly influenced the plastic deformation, ductility, and strength. For samples deforming under a lower loading speed, the results had a large plastic deformation region and a lower point. As the speed increased, PLA behaved more brittle and stiffer but showed no significant difference after 508 mm/min. Therefore, although the actual impact speed is much higher than the instrument limit, the data under the speed of 1270 mm/min was considered converged to represent the properties of the PLA frame under high strain rates.

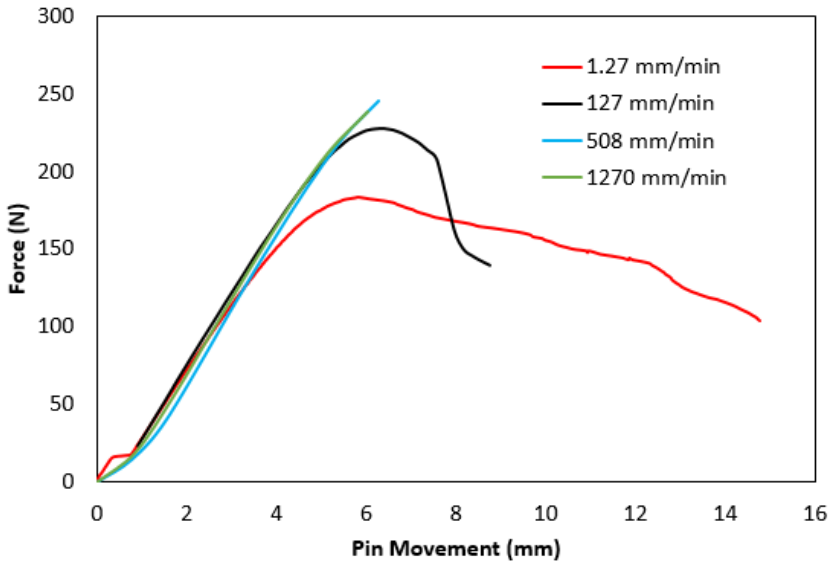

Figure 33 The strain rate effect of the PLA structure under 3-point bending test

The properties to be determined by the inverse method included the modulus of elasticity and strength. Each parameter was searched based on the two-digit accuracy Golden Section method with the least-square regression fitting. Note that an isotropic material was assumed despite the anisotropy of actual 3D printed parts because the dominant modulus is in X-direction in bending (Fig. 32) and the test configuration is the same as the impact experiment. Similarly, although the strength can be anisotropic, the structure would always fail when the stress reaches the lowest tolerable strength. Thus, only one strength is needed to describe the behavior before the structural damage. However, unlike a typical ductile material, a printed PLA does not have the same tensile and compressive strengths. According to Y. Song et al. [98], the compressive strength is about 1.75 times higher under a strain rate of 2.5 × 10-4 s-1. Since the ductile material model in FEA generally cannot define different tensile and compressive strengths, the PLA frame was separated into two sections in the FEA model (Fig. 32), where the top section was defined with the same modulus but higher strength. Note that, a higher compressive strength does not affect the maximum force at structural failure because the tensile strength is reached first on the bottom section. However, this step is necessary because, without a higher compressive strength in the top layer, the lattice structure fails from the top due to a high strain rate contact in the simulation, which is not seen in any of impact tests (Fig. 35). Based on the inverse results, the obtained modulus is 2300 MPa, and tensile strength is 64 MPa. The compressive strength is set as 112 MPa (1.75 times higher than the tensile one).

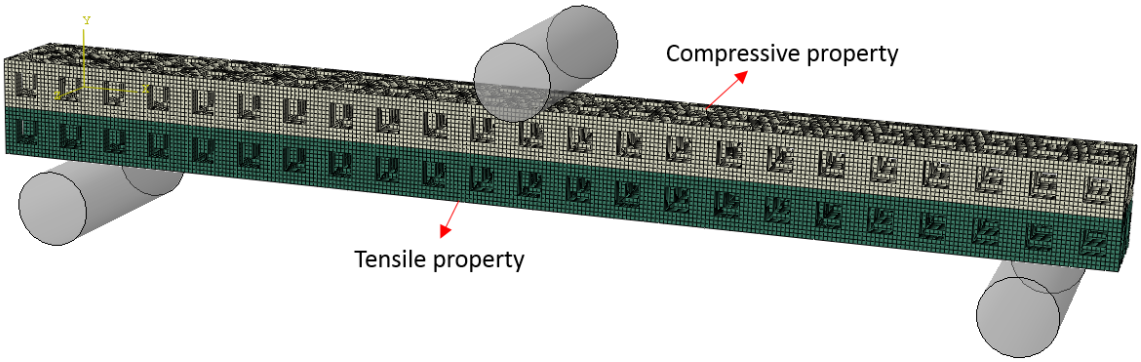

Figure 34 The FEA model configuration for 3D printed frame

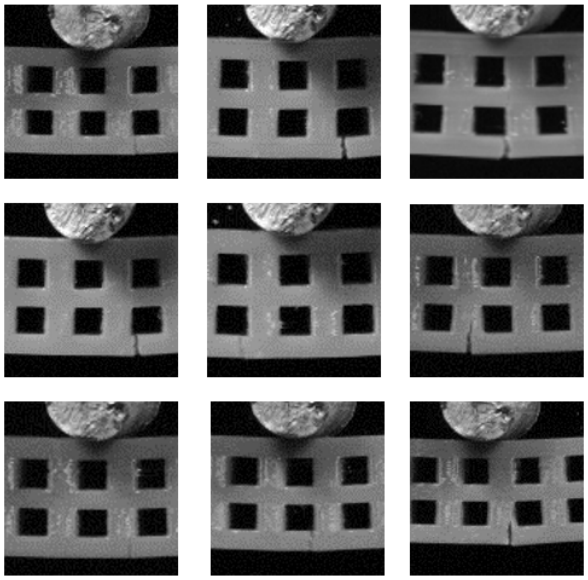

Figure 35 High speed images of 3D printed PLA frame at the initial failure

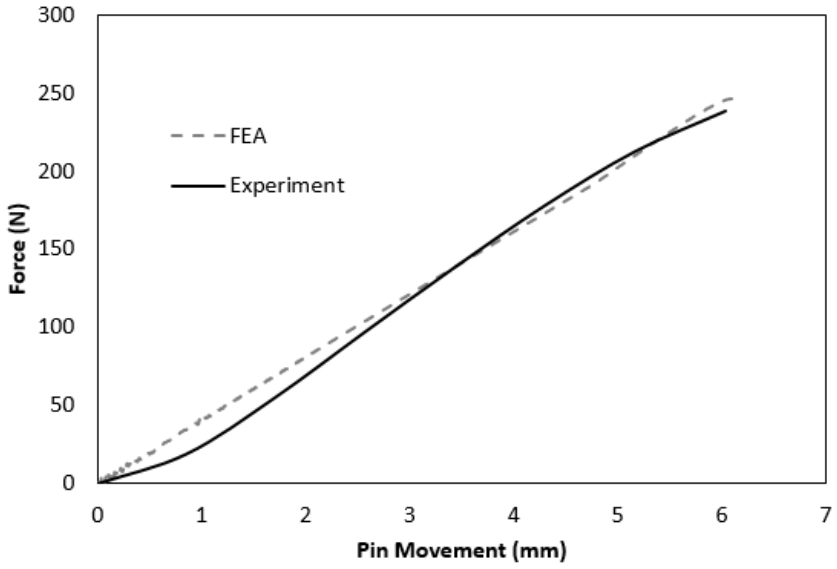

Figure 36 The comparison between the FEA and experiment three-point bending test

5.2.3. PU foam

The PU foam is modeled by the Prony-series viscoelastic model. The Prony series is determined by a compressive stress relaxation test on a universal test system (MTS Insight 30) following the ASTM E328 [6] for a 20 mm diameter and 40 mm height cylindrical PU sample. In the experiment, the foam cylinder sample was rapidly compressed to 9% strain and remained at the same strain level to measure the relaxation modulus. The Generalized Maxwell model for the curve fitting is shown in Eq. (5)

$$E(t) = E_0 + E_1 e^{-t/\tau 1} + E_2 e^{-t/\tau 2} + E_3 e^{-t/\tau 3} \quad (5)$$

where $E(t)$ is the elastic modulus at time t, E_0 is the long-term elastic modulus, E_i is the material constants, and τ_i represent the relaxation time. The obtained parameters are listed in Table. 3 through the curve fitting shown in Fig. 37. The Poisson's ratio of PU foam is

assumed a constant value (0.33) because the expected deformation is small. In addition, since the frame will always fail before the PU foam, damage criteria of the foam are not considered.

Table 3 The obtained parameters of the Maxwell model

Variables	Parameters
E_0 (MPa)	0.6185
E_1 (MPa)	0.1379
E_2 (MPa)	0.0812
E_3 (MPa)	0.1080
$\tau 1$	0.3509
$\tau 2$	21.8627
$\tau 3$	2.6337

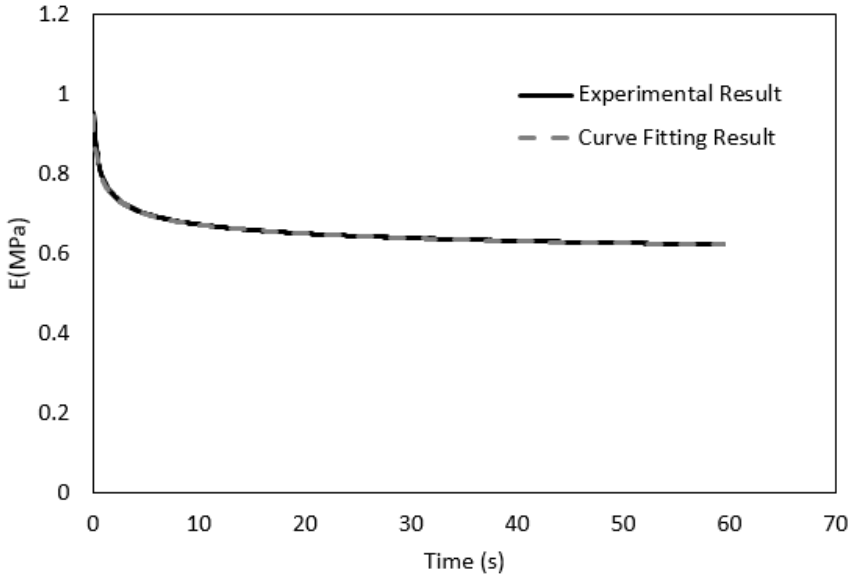

Figure 37 The comparison between the relaxation test and the curve fitting result

5.3. Model sensitivity analysis

This section presents the sensitivity study of multiple assumptions used to simplify the model, including mesh size, compressive strength, and Poisson's ratio to ensure the model robustness.

5.3.1. Mesh size

The mesh size of 0.40625 mm was used in the simulation model. To ensure a proper mesh, the convergence study was conducted on the composite model based on the acceleration data at the top pin (i.e., the impactor). Different mesh sizes of 0.8125 mm, 0.40625 mm, 0.2708 mm, and 0.2031 mm were tested, and the results are overlaid in Fig. 38 throughout the impact duration. All cases have a similar acceleration response. Although a finer mesh tends to increase the failure time (from 0.003354 to 0.003498 s), the difference is minimal compared to the entire impact duration. The failure point change is less than 0.000064 s after the mesh size is down to 0.40625 mm. Note that, such a large fluctuating data is normal because of the vibration of the structure reacting on the impactor pin.

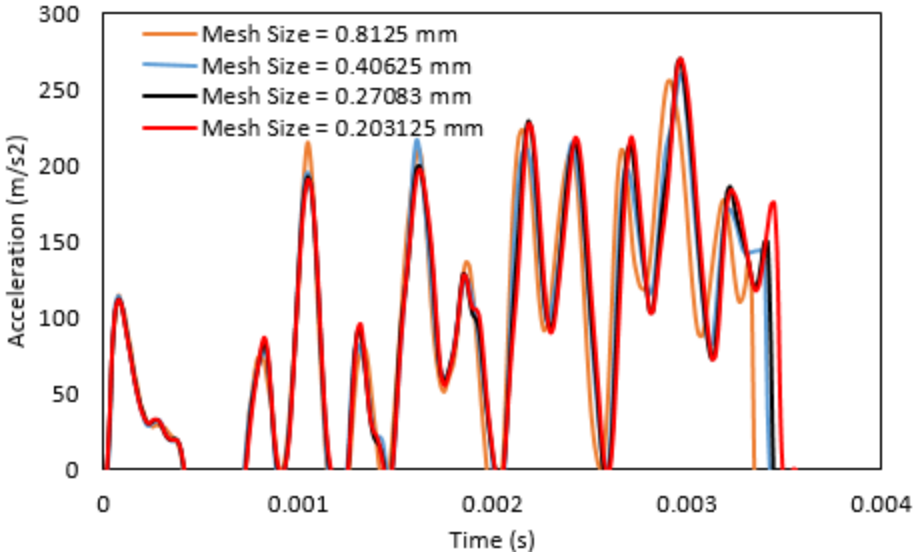

Figure 38 The mesh convergence test of the *type II* composite model

5.3.2. Compressive strength

As mentioned in Section 5.2, the top section of the PLA frame is defined with a higher compressive strength to prevent unrealistic failure from the local deformation and stress concentration at the impactor-workpiece contact. The value of 1.75 was adopted from a published work, but it could vary from one case to another. Although this value should theoretically not change the structural response (as the modulus remains the same) nor the failure point at the tension section, a sensitivity study was conducted to confirm that this scaling factor had no direct effect on the acceleration data. Fig. 39 shows the results with the factor ranging from 1.5 to 3. As seen, adding a scaling factor for the compressive strength has no effect on the structural response to the impact.

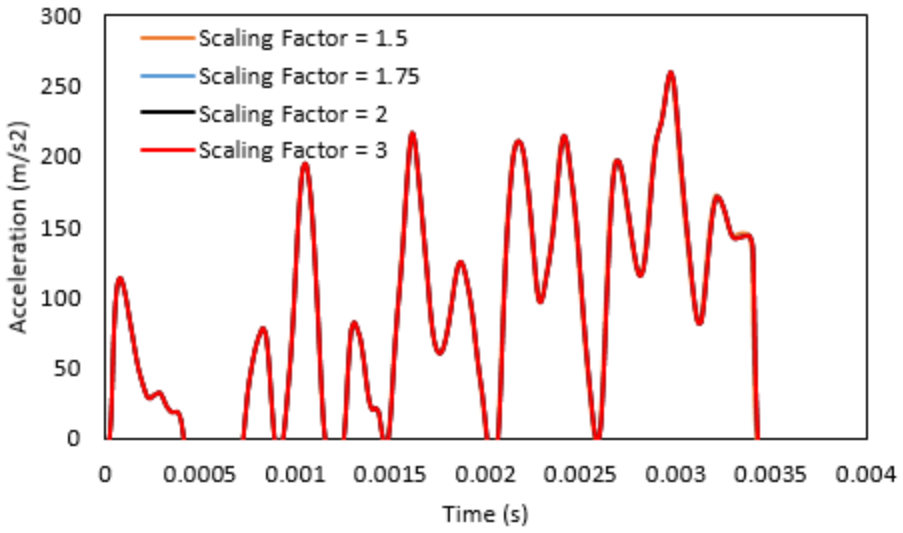

Figure 39 The compressive yield strength scaling factor sensitivity test of the 3D printed PLA lattice structural model

5.3.3. Poisson's ratio

The Poisson's ratio of PU foams is usually a non-linear function of strain [99], but it was assumed to be a constant in the model under the assumption of small deformation inside the composite structure. To ensure this constant ratio not to affect the acceleration data, different Poisson's ratios (0.2, 0.33, and 0.49) were tested and compared. As shown in Fig. 40, the difference among acceleration-time curves of different Poisson's is nearly none, which proves that the effect is negligible in this particular case. This can be explained by the fact that the stiffness of the PU foam is much lower than that of the 3D printed PLA, so the PLA frame dominates the overall mechanical stiffness regardless of the stress variation as a result of the Poisson's ratio.

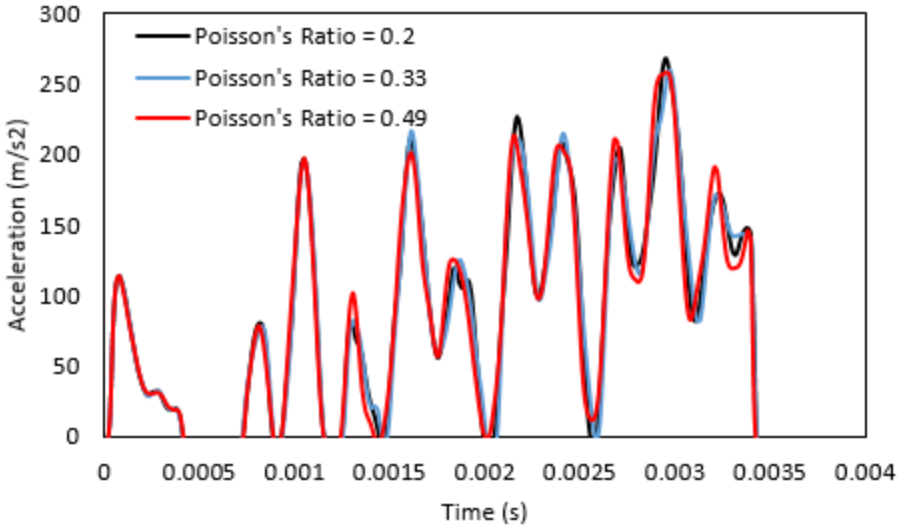

Figure 40 The sensitivity test of the PU foam's Poisson's ratio

5.4. Model results and comparison with experimental data

In this section, FEA-simulated acceleration data is compared with the experimental data to validate the model, and then the model is used to explain the underlying mechanism of the improved impact properties.

5.4.1. Acceleration response

The acceleration-time (a-t) data from FEA models of the PLA frame and the composite are shown in Figs. 41(a) and (b), respectively, and they are overlaid on 10 individual experimental data from the drop-weight test. To be noted that, unlike the FEA data in the sensitivity study, the data here are filtered by using the Butterworth method to be consistent with the experiments. In the experiments, raw data contained not only structural vibration but various noises from the system and environment, leading to the difficulty in

distinguishing the differences. Filtering was necessary for the experimental study to see the acceleration change and to measure the impact performance quantitatively.

In Figs. 41(a) and (b), the red line represents the averaged failure point of all experimental tests, and the green lines, σ, represent one standard deviation from the average. The failure point of both FEA models falls within one standard deviation range of the experimental data. The failure time indicates the structural deformation and ductility. It is clear that, after adding the foam, the structure possesses extended impact tolerance. The predicted extension in FEA was from 0.00326 s to 0.00347 s (about 6.4% increase), while that from the experiments was 0.00319 s to 0.00367 s (about 15% increase), on average.

The maximum acceleration and acceleration rate of the FEA data were both lower than that of the experimental data, which imply that the modulus of the PLA frame obtained from the inverse method may be underestimated with the loading rate used. Nonetheless, the discrepancy in modulus does not necessarily affect the failure point prediction since the impactor has a sufficient momentum not to be slowed down by the stiffness of the frame structure. In other words, the impact duration (i.e., structural deflection rate) is the same regardless of the modulus. Overall, the a-t curves of both FEA and experiments show a similar trend during the impact tests.

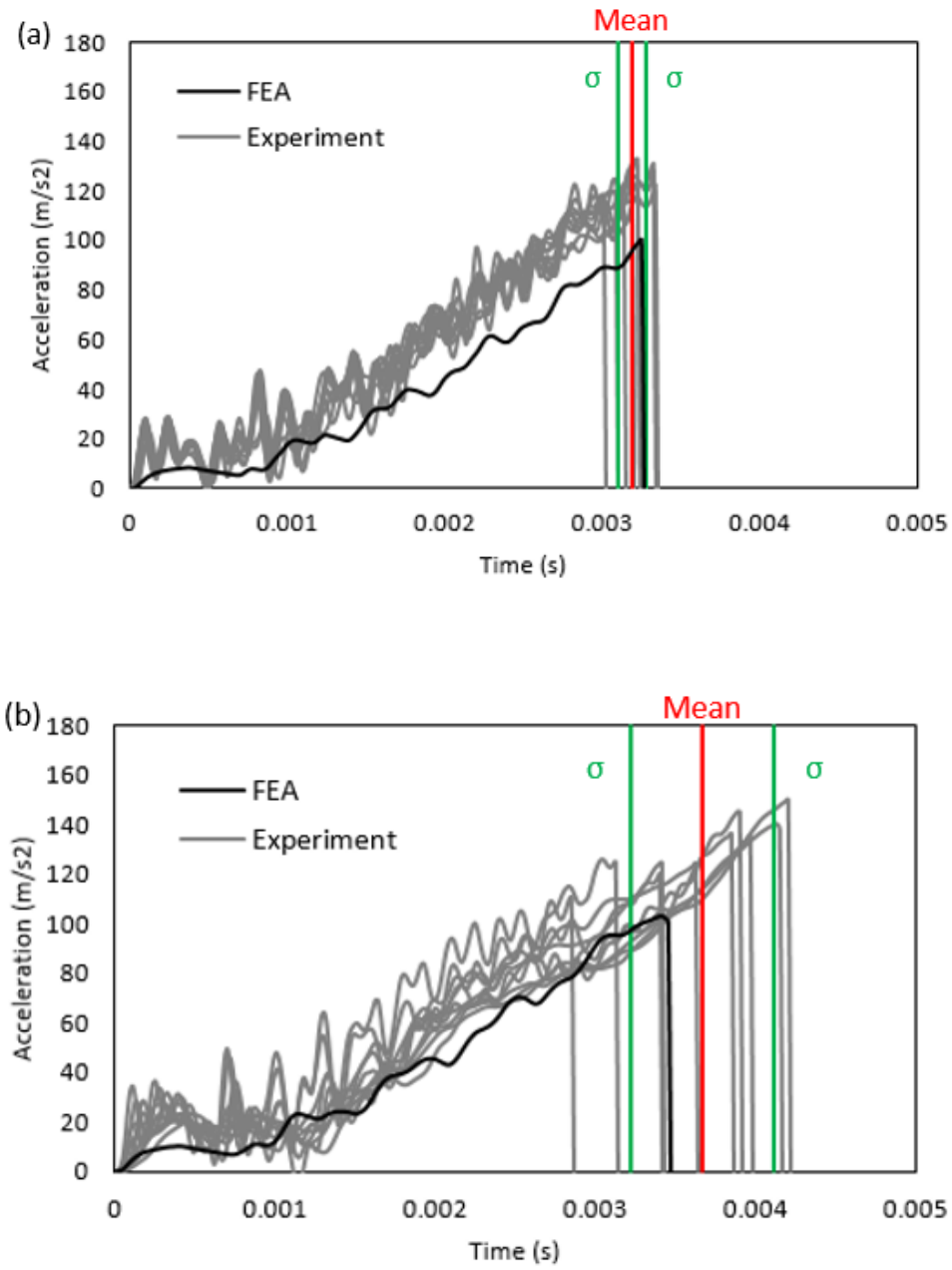

Figure 41 Acceleration-time curves (a) 3D printed PLA lattice structure (b) *type II* composite

5.4.2. Impact properties

Four measures are used to describe impact performance include maximum deflection, maximum acceleration, energy absorption, and jerk (acceleration rate), which are termed impact properties. The maximum deflection indicates the structural ductility; the maximum acceleration indicates the impact force. The energy absorption represents the structural impact toughness; the jerk indicates the attenuation of an impact shock. These four properties are obtained by the *a-t* curve and the force-deflection curve integrated from the *a-t* data [74].

Figure 42 shows the results of the maximum deflection before structural failure between the experiment and FEA. The experiment shows that, after adding PU foam into the PLA lattice structure, the maximum deflection increases by 1.13 mm (17%), which implies a more ductile behavior of the structure. While the increase of deflection is only about 0.51 mm (7.5%) in FEA, it falls in the 95% confident interval of the experimental data considering the variations. Despite the small discrepancy, the phenomenon of delayed failure can be captured by the FEA model.

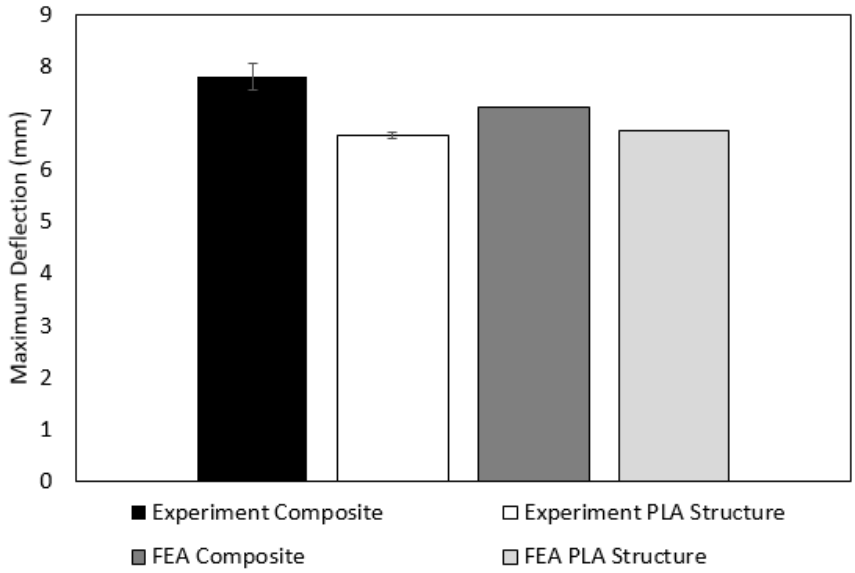

Figure 42 The maximum deflection of the *type II* composite and the PLA lattice structure

The results of the maximum acceleration are shown in Fig. 43. The experiment shows a 9.7 m/s2 increase (7.6%) after adding the foam, though the difference was not statistically significant. The FEA shows a similar increasing trend in the maximum acceleration by 2.44 m/s2 (2.4 %), but FEA had a lower level of acceleration compared to that of the experiments. This may be due to an underestimated modulus of PLA material from the inverse method, which leads the structure to behave less stiff. Nonetheless, the modulus discrepancy does not affect the overall structural behavior because of nearly no momentum change of the impactor during the test. In other words, the displacement-time curves are nearly identical between the experiment and FEA (as evidenced in Fig. 42). Thus, a larger acceleration is a definite result of the greater deflection (Fig. 42).

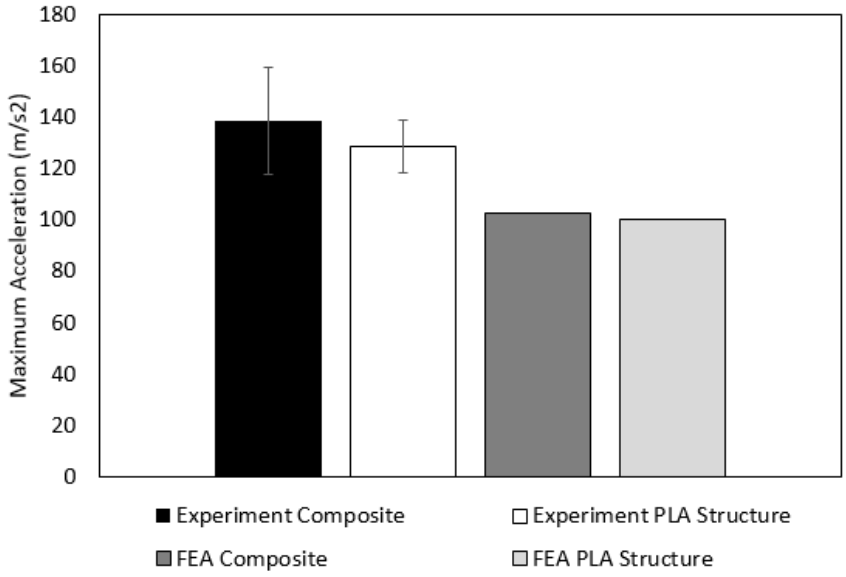

Figure 43 The maximum acceleration of the *type II* composite and the PLA lattice structure

Figure 44 shows the results of energy absorption obtained by the integrated force-displacement curve. After adding the foam, the energy absorption increased by 0.11 N·m (21.6%) in the experiment and 0.06 N·m (17%) in FEA. The increase in energy absorption is the consequence of both higher deflection and maximum force (acceleration) taken by the composite structure as shown by Fig 42 and Fig. 43 respectively. The lower magnitude of energy absorption in the FEA model is due to the accumulation of the underestimated acceleration data in Fig. 43.

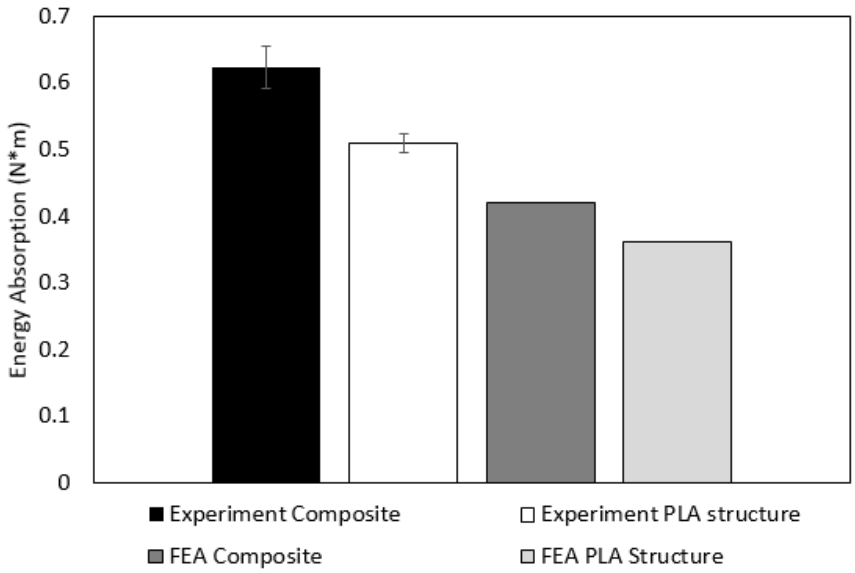

Figure 44 The energy absorption of the *type II* composite and the PLA lattice structure

For the results of the jerk (Fig. 45), interestingly, the foam had an opposite effect between the experiment and FEA. Adding the foam decreases the jerk by about 7% in the experiment. However, in FEA, the jerk increased by 2%. In theory, the rate of acceleration should always be proportional to the stiffness of the object. The softer the object is, the less the acceleration changes. Therefore, the jerk should always be higher, as described in FEA, whenever there is additional material in the structure. The opposite experimental result, though small, may be due to the imperfection of samples. As shown in Fig. 31 (a), a thin layer of PU foam is formed around the cellular structure that leads to the effect of jerk reduction.

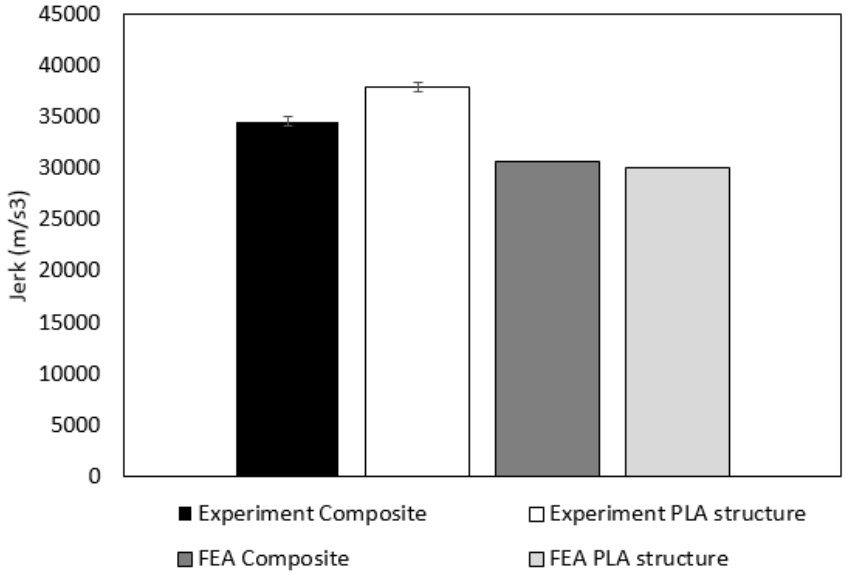

Figure 45 The jerk of the *type II* composite and the PLA lattice structure

5.4.3. Stress distribution analysis

Stress distribution was visualized to explain the reason behind the improved impact properties. Since the impact is a highly dynamic event where the structure not only bends but also vibrates during the impact, the stress distribution can fluctuate both temporally and spatially, resulting in difficulty comparing two structures at a certain time or displacement. Therefore, two characteristic points, initial bending stage and fracture, are identified for a fair comparison, as shown in Fig. 46(a). The initial bending stage is defined at the first peak of the *a-t* curve. That is, a pure bending occurs during this initial bending stage. Fracture is defined at the point right before the structural failure and acceleration drops to zero. The stress distribution is compared at the center region of the bar from the front and bottom views, as shown in Fig. 46(b).

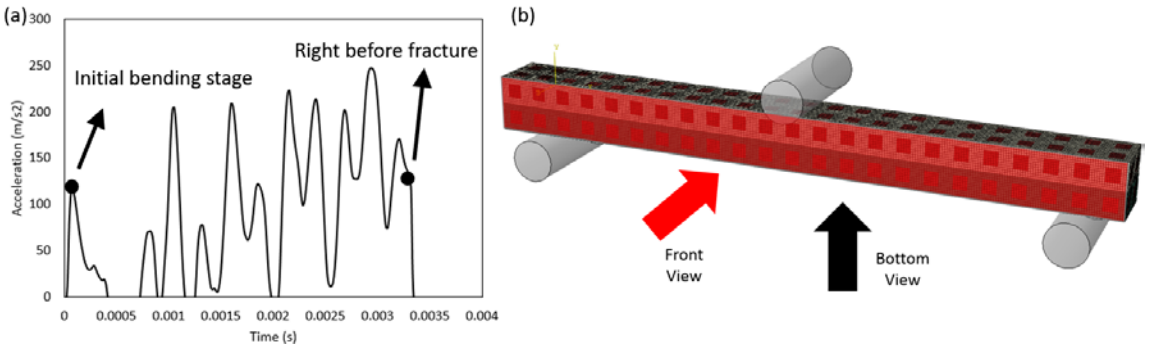

Figure 46 (a) The definition of initial bending stage and the point right before the fracture (b) the definition of front view and bottom view

Von Mises stress map was created at the initial bending stage, as shown in Fig. 47. Figures on the top row are the composite material, and those on the bottom row are the PLA lattice structure. From both the side and the bottom views, the stress distribution patterns were similar between the two cases. However, the lattice structure had more high-stress areas (in the grey color) compared to the composite, especially from the bottom view. Also, the maximum stress level of the lattice structure was around twice higher than that of the composite, which occurred at the impactor-sample contact area. All these observations indicate that the foam material redistributes the stress in the composite during impact.

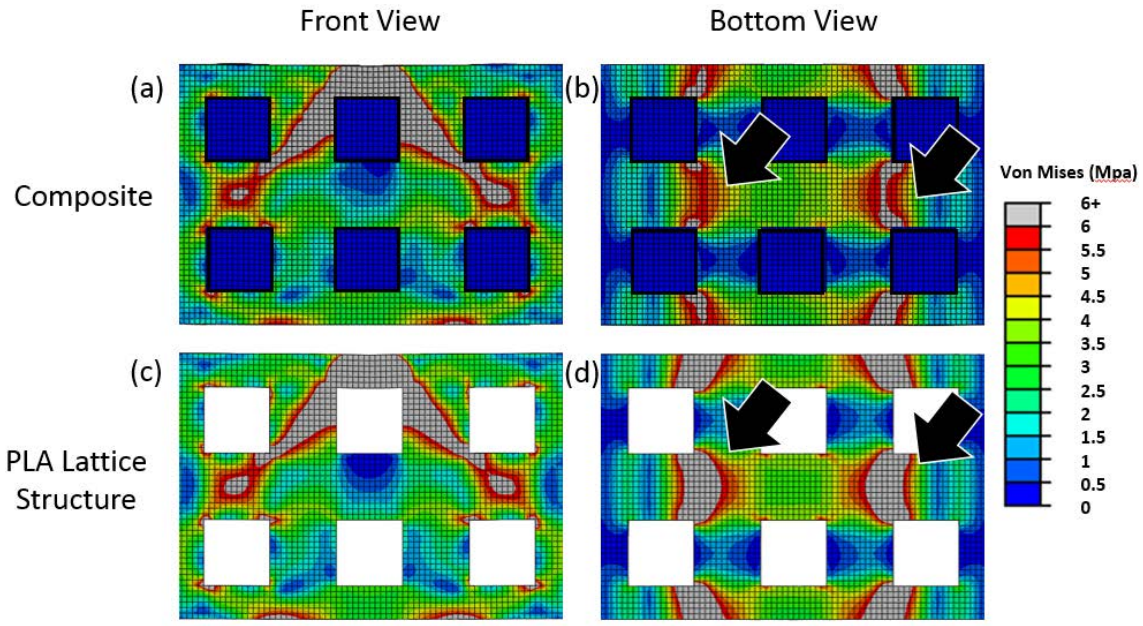

Figure 47 The stress distribution under the initial impact (a) *Type II* composite – front view (b) *Type II* composite – bottom view (c) PLA lattice structure – front view (d) PLA lattice structure – bottom view

To further confirm the foam redistributing, rather than taking, the stress acting on the frame, Fig. 48 shows the stress distributions of the two constituent materials in the composite individually at the initial bending stage. For the foam material (Fig. 48(a)), the maximum Von Mises stress was 0.054 MPa, while that of the PLA lattice structure part, was 38.49 MPa (Fig. 48(b)), which was significantly higher than the foam material. This substantial difference indicates that the foam material does not share much load from the frame; instead, the network of the PU foam allows to bridge the open areas in the lattice structure and redistribute the stress in the frame (Fig. 47).

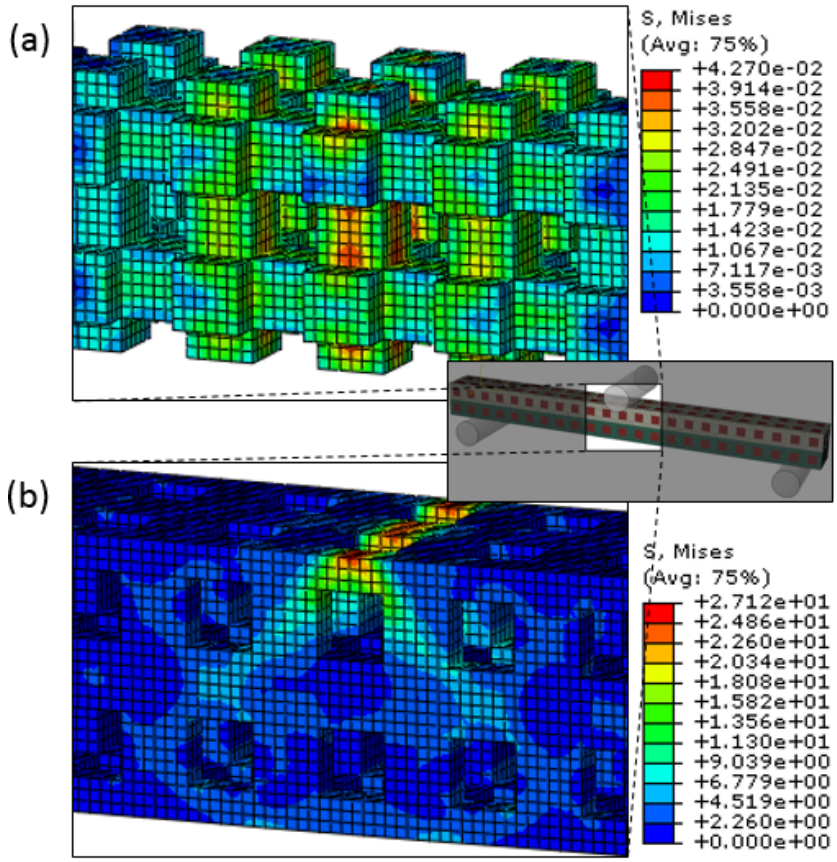

Figure 48 Mechanical responses of the composite material (a) the foam material part inside the *type II* composite (b) the PLA lattice frame part inside the *type II* composite

The stress distribution immediately before the fracture of the PLA lattice structure and the composite are shown in Fig. 49. To be noted that, the foam-filled composite deflects more than the PLA frame before it fails. It can be seen that, at the onset of fracture, the stress distribution of the composite was more even than that of the PLA lattice structure. The bottom view of the PLA frame (Fig. 49(d)) shows large stress variation across the center web. It is evidenced that the foam redistributes the stress inside the structure. This

observation also explains the reason why the composite can take more deflection before it fractures (Fig. 42). Also, since the composite tolerates more deflection, a higher maximum force (Fig. 43) is needed to fracture the specimen.

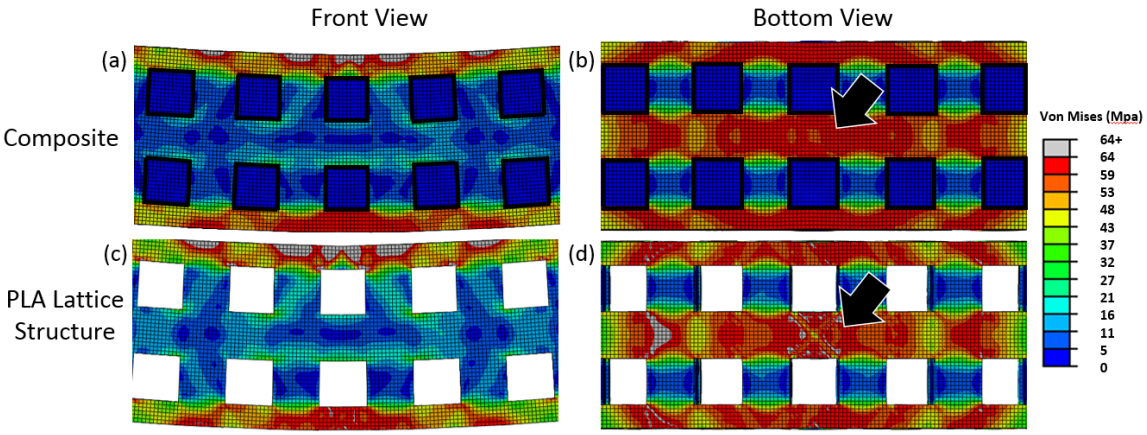

Figure 49 The stress distribution immediately before the fracture (a) *Type II* composite – front view (b) T*ype II* composite – bottom view (c) PLA lattice structure – front view (d) PLA lattice structure – bottom view

5.5. Model limitations

The following limitations are applied to this model, but they do not necessarily influence the results obtained. First, there are no failure criteria specified for the foam material. The fracture of the composite includes three steps, crack initiation, crack propagation, and the fracture. Since the post-failure behavior is not currently of interest, the FEA model only predicts the step of crack initiation (on the frame) due to the complexity in modeling foam degradation and failure. Second, the mechanical properties for the 3D printed PLA do not represent the directionality, interlayer bonding, and strain-rate dependency. However, since equivalent modulus and strength are determined by the

inverse method with an identical bending configuration, they are sufficient to describe the structural behavior. Certainly, for more general simulation or other impact configurations, these properties should be measured experimentally. Lastly, the inconsistency and resolution of 3D printing are not taken into account. The FEA model was built based on the CAD model, while the actual printed part might contain geometrical imperfection, especially in small features. These errors could cause simulation discrepancy. It should be noted that the current FEA model is not a complete mechanistic model to predict all elastic and non-elastic behavior, material degradation, and failure; instead, it is aimed to explain how a PU foam can enhance the integrity of the composite structure under a low-velocity impact.

5.6. Conclusions

This chapter used FEA to explain the foam reinforcement effect of the 3D printed lattice composite under a low-velocity impact. An elastic material model was applied to the 3D printed PLA frame, and a viscoelastic material model was applied to the PU foam material. The FEA results suggest that, although the modulus of the foam material is significantly lower than the PLA (in the order of three), it can redistribute the stress during impact. In other words, the PU foam does not enhance the total stiffness and strength directly, but it extends the failure of the structure by tolerating more deflection, thereby enhancing the total energy absorption. The future work will be focused on addressing the limitations of the current model and incorporate interactions between the two constituent materials.

6. CONCLUSIONS AND FUTURE WORK

6.1. Conclusions and Major Contributions

This dissertation studied the manufacturing methods and the mechanical responses of the 3D printed composite materials under quasi-static and low-velocity bending conditions by using both experimental and numerical methods. Two different composites were included in this study. *Type I* composite consisting of a 3D printed brittle ceramic frame and impregnated with elastomer material in order to enhance the material toughness. *Type II* composite consisting of 3D printed ductile frame and reinforced with PU foam in order to improve the impact performance. Overall, this dissertation provides knowledge of manufacturing, testing, and analyzing the 3D printed composites.

Major contributions of this dissertation can be summarized as follows:

I. Conventionally, the manufacturing processes of the structural composite are complicated. The proposed method in this study, using 3D printing technologies can possibly simplify the manufacturing processes and enable a more complex structural design for engineering applications.

II. The proposed composite materials show the advantages of incorporating another material to improve the toughness and impact resistance. Traditional composite can only be modified by the volume ratio and 2D design (laminate orientation). With using the 3D printing technologies, the composite materials can have more degree of freedom in design to be customized toward specific applications, such as anisotropic property and localized strength.

III. The current study also explains the material responses under both quasi-static and impact tests. The material phenomena inside the structural composite material can be very complicated, and it significantly affects the material performance under deformation. The proposed numerical models can be used to explain material phenomena and improve the future design.

This dissertation provides a broad knowledge of 3D printed composite, and it is beneficial for engineering industries. The conclusions and significant findings can be summarized as follow:

1. Combining the 3D printing technologies and molding process can successfully manufacture the structural composite. Comparing to the conventional methods, this manufacturing process provides more options on the material, such as concrete and plaster, which traditionally cannot be made with complicated geometries. Also, with 3D printing technologies, creating a complex structural composite becomes more accessible than the traditional methods, such as welding and adhesions. The composites with anisotropic or localized design can be easily made with the proposed manufacturing method.
2. The mechanical properties of 3D printed structural composites are determined by both the volume fraction and structural configurations. With the extremely different properties of the materials and the 3D printing technologies, a composite with a wide range of the mechanical properties can be customized for specific applications.

3. *Type I* composite consisted of a brittle 3D printed plaster frame and impregnate with a ductile silicone elastomer. The 3D printed plaster frame dominates the stiffness and the strength, and the elastomer enhances the material toughness. Both experimental and numerical studies show that the composite does not rupture suddenly because of the gradual development of the microcracks in the ceramic phase as a result of contraction force provided by the elastomer filler. The loading-unloading study showed that there are stiffness degradation and minimal permanent deformation on the *type I* composite after each cycle. This also proves that the microcracks evolution occurs in the *type I* composite.
4. The bending behaviors of the *type I* composite were successfully modeled using an FEA method, which includes a brittle cracking model for the ceramic phase material and a hyperelastic model for the elastomer phase material. Comparing to other conventional FEA models, this model enabled the analysis with coarse and uniform mesh in the structure to represent the crack evolution inside the material.
5. *Type II* composite consisted of a 3D printed PLA frame and reinforced with a PU foam material. The impact testing results showed that different foams affect the impact properties differently and do not always show the improvement. The flexible foam can enhance the material ductility and absorb more energy during the impact. In addition, the flexible foam stabilizes the crack propagation; in other words, it slows down the crack propagation speed.

6. The impact behaviors of *type II* composite can be captured by an FEA model, which includes an elastoplastic model for the PLA frame and a viscoelastic model for the PU foam. The FEA results suggest that although the PU foam has a significantly lower modulus compared to that of the PLA, it redistributes the stress and mitigates stress concentrations during impact. Consequently, the PU foam reinforcement enhances the material ductility without changing its structural stiffness and weight significantly because of the soft and light nature of foams. Such characteristic is an advantage for future composite design.

6.2. Future Works

The proposed manufacturing process of the composite material, the numerical models, and the composite design for specific applications can all be improved. Future research can follow the following directions:

1. The proposed manufacturing method in this study includes both 3D printing and molding process. In the future, a 3D printer can print multiple materials with extremely different properties will significantly increase the degree of freedom for the composite design.
2. This study proved that the structural configuration significantly affects material properties. An algorithm to design the composite structure for specific applications and needs will significantly improve the material properties. The optimization needs to consider both material properties and frame structure because of their coupled effects on mechanical behaviors.

3. A failure model for the soft and ductile material needed to be developed. In this study, both of the FEA models do not include a failure criterion for the reinforcement material (elastomer and PU foam). According to the impact testing results, selecting a proper PU foam as the reinforcement material can slow down the crack propagation in the composite. If the numerical model can capture the mechanism, the future composite design can be improved.

REFERENCES

[1] Conner BP, Manogharan GP, Martof AN, Rodomsky LM, Rodomsky CM, Jordan DC, et al. Making sense of 3-D printing: Creating a map of additive manufacturing products and services. Additive Manufacturing. 2014;1:64-76.
[2] Huang SH, Liu P, Mokasdar A, Hou L. Additive manufacturing and its societal impact: a literature review. The International Journal of Advanced Manufacturing Technology. 2013;67:1191-203.
[3] Guo N, Leu MC. Additive manufacturing: technology, applications and research needs. Frontiers of Mechanical Engineering. 2013;8:215-43.
[4] Kumar S, Kruth J-P. Composites by rapid prototyping technology. Materials & Design. 2010;31:850-6.
[5] Nikzad M, Masood SH, Sbarski I, Groth AM. Rheological properties of a particulate-filled polymeric composite through fused deposition process. Materials Science Forum: Trans Tech Publ; 2010. p. 2471-4.
[6] Shofner M, Lozano K, Rodríguez-Macías F, Barrera E. Nanofiber-reinforced polymers prepared by fused deposition modeling. Journal of applied polymer science. 2003;89:3081-90.
[7] Kernan BD, Sachs EM, Oliveira MA, Cima MJ. Three-dimensional printing of tungsten carbide–10 wt% cobalt using a cobalt oxide precursor. International Journal of Refractory Metals and Hard Materials. 2007;25:82-94.
[8] Cao S, Wei X-F, Sun Z-J, Zhang H-H. Investigation on urea-formaldehyde resin as an in-powder adhesive for the fabrication of Al2O3/borosilicate–glass composite parts by three dimensional printing (3DP). Journal of Materials Processing Technology. 2015;217:241-52.
[9] Rambo C, Travitzky N, Zimmermann K, Greil P. Synthesis of TiC/Ti–Cu composites by pressureless reactive infiltration of TiCu alloy into carbon preforms fabricated by 3D-printing. Materials Letters. 2005;59:1028-31.
[10] Popov V, Evseev A, Ivanov A, Roginski V, Volozhin A, Howdle S. Laser stereolithography and supercritical fluid processing for custom-designed implant fabrication. Journal of Materials Science: Materials in Medicine. 2004;15:123-8.
[11] Melchels FP, Feijen J, Grijpma DW. A review on stereolithography and its applications in biomedical engineering. Biomaterials. 2010;31:6121-30.
[12] Wang F, Mei J, Wu X. Compositionally graded Ti6Al4V+ TiC made by direct laser fabrication using powder and wire. Materials & Design. 2007;28:2040-6.
[13] Syed WUH, Pinkerton AJ, Li L. Combining wire and coaxial powder feeding in laser direct metal deposition for rapid prototyping. Applied surface science. 2006;252:4803-8.
[14] Uddin MN, Gandy HTN, Rahman MM, Asmatulu R. Adhesiveless honeycomb sandwich structures of prepreg carbon fiber composites for primary structural applications. Advanced Composites and Hybrid Materials. 2019;2:339-50.
[15] Sigl LS, Mataga P, Dalgleish B, McMeeking R, Evans A. On the toughness of brittle materials reinforced with a ductile phase. Acta Metallurgica. 1988;36:945-53.
[16] Mataga PA. Deformation of crack-bridging ductile reinforcements in toughened brittle materials. Acta Metallurgica. 1989;37:3349-59.

[17] Wu H, Fan G, Huang M, Geng L, Cui X, Xie H. Deformation behavior of brittle/ductile multilayered composites under interface constraint effect. International Journal of Plasticity. 2017;89:96-109.
[18] Zhang G, Wang B, Ma L, Wu L, Pan S, Yang J. Energy absorption and low velocity impact response of polyurethane foam filled pyramidal lattice core sandwich panels. Composite Structures. 2014;108:304-10.
[19] Gustin J, Joneson A, Mahinfalah M, Stone J. Low velocity impact of combination Kevlar/carbon fiber sandwich composites. Composite Structures. 2005;69:396-406.
[20] Hosur MV, Abdullah M, Jeelani S. Manufacturing and low-velocity impact characterization of foam filled 3-D integrated core sandwich composites with hybrid face sheets. Composite Structures. 2005;69:167-81.
[21] Zhang G, Wang B, Ma L, Xiong J, Wu L. Response of sandwich structures with pyramidal truss cores under the compression and impact loading. Composite Structures. 2013;100:451-63.
[22] George T, Deshpande VS, Wadley HN. Mechanical response of carbon fiber composite sandwich panels with pyramidal truss cores. Composites Part A: Applied Science and Manufacturing. 2013;47:31-40.
[23] Queheillalt DT, Murty Y, Wadley HN. Mechanical properties of an extruded pyramidal lattice truss sandwich structure. Scripta Materialia. 2008;58:76-9.
[24] Bouwhuis B, Hibbard G. Compression testing of periodic cellular sandwich cores. Metallurgical and Materials Transactions B. 2006;37:919-27.
[25] Côté F, Fleck N, Deshpande V. Fatigue performance of sandwich beams with a pyramidal core. International journal of fatigue. 2007;29:1402-12.
[26] Wong KV, Hernandez A. A review of additive manufacturing. ISRN Mechanical Engineering. 2012;2012.
[27] Leong C, Lu L, Fuh J, Wong Y. In-situ formation of copper matrix composites by laser sintering. Materials Science and Engineering: A. 2002;338:81-8.
[28] Klosterman D, Chartoff R, Graves G, Osborne N, Priore B. Interfacial characteristics of composites fabricated by laminated object manufacturing. Composites Part A: Applied Science and Manufacturing. 1998;29:1165-74.
[29] Domack M, Baughman J. Development of nickel-titanium graded composition components. Rapid Prototyping Journal. 2005;11:41-51.
[30] Chung H, Das S. Processing and properties of glass bead particulate-filled functionally graded Nylon-11 composites produced by selective laser sintering. Materials Science and Engineering: A. 2006;437:226-34.
[31] Krishna BV, Xue W, Bose S, Bandyopadhyay A. Functionally graded Co–Cr–Mo coating on Ti–6Al–4V alloy structures. Acta biomaterialia. 2008;4:697-706.
[32] Gagel A, Lange D, Schulte K. On the relation between crack densities, stiffness degradation, and surface temperature distribution of tensile fatigue loaded glass-fibre non-crimp-fabric reinforced epoxy. Composites Part A: Applied Science and Manufacturing. 2006;37:222-8.
[33] Lee J, Fenves GL. Plastic-damage model for cyclic loading of concrete structures. Journal of engineering mechanics. 1998;124:892-900.

[34] Flores-Johnson E, Li Q, Mines R. Degradation of elastic modulus of progressively crushable foams in uniaxial compression. Journal of Cellular Plastics. 2008;44:415-34.
[35] Kao Y-T, Zhang Y, Wang J, Tai BL. Bending behaviors of 3D-printed Bi-material structure: Experimental study and finite element analysis. Additive Manufacturing. 2017;16:197-205.
[36] D. A. Standard test method for flexural properties of polymer matrix composite materials. American Society for Testing and Materials Annual Book of ASTM Standards. 2007.
[37] Kao Y-T, Zhang Y, Wang J, Tai BL. Loading–Unloading Cycles of Three-Dimensional-Printed Built Bimaterial Structures With Ceramic and Elastomer. Journal of Manufacturing Science and Engineering. 2017;139:041006.
[38] Berthelot J-M, Ling FF. Composite materials: mechanical behavior and structural analysis: Springer, 1999.
[39] Kreja I. A literature review on computational models for laminated composite and sandwich panels. Open Engineering. 2011;1:59-80.
[40] Zhang Y, Yang C. Recent developments in finite element analysis for laminated composite plates. Composite Structures. 2009;88:147-57.
[41] Swaminathan S, Ghosh S, Pagano N. Statistically equivalent representative volume elements for unidirectional composite microstructures: Part I-Without damage. Journal of Composite Materials. 2006;40:583-604.
[42] Harper L, Qian C, Turner T, Li S, Warrior N. Representative volume elements for discontinuous carbon fibre composites–Part 1: Boundary conditions. Composites Science and Technology. 2012;72:225-34.
[43] Spanos K, Georgantzinos S, Anifantis N. Investigation of stress transfer in carbon nanotube reinforced composites using a multi-scale finite element approach. Composites Part B: Engineering. 2014;63:85-93.
[44] Xi Y. Representative volumes of composite materials. Journal of engineering mechanics. 1996;122:1159-67.
[45] Tabiei A, Jiang Y. Woven fabric composite material model with material nonlinearity for nonlinear finite element simulation. International Journal of Solids and Structures. 1999;36:2757-71.
[46] Liu Y, Chen X. Evaluations of the effective material properties of carbon nanotube-based composites using a nanoscale representative volume element. Mechanics of materials. 2003;35:69-81.
[47] Chen X, Liu Y. Square representative volume elements for evaluating the effective material properties of carbon nanotube-based composites. Computational Materials Science. 2004;29:1-11.
[48] Systèmes D. Abaqus 6.14 Documentation. Providence, RI: Dassault Systèmes. 2014.
[49] Costin L. Damage mechanics in the post-failure regime. Mechanics of materials. 1985;4:149-60.
[50] Song J-H, Wang H, Belytschko T. A comparative study on finite element methods for dynamic fracture. Computational Mechanics. 2008;42:239-50.
[51] Tungjitkusolmun S, Woo E, Cao H, Tsai J, Vorperian V, Webster J. Thermal—electrical finite element modelling for radio frequency cardiac ablation: effects of changes

in myocardial properties. Medical and Biological Engineering and Computing. 2000;38:562-8.
[52] Joldes GR, Wittek A, Miller K. Real-time nonlinear finite element computations on GPU–Application to neurosurgical simulation. Computer methods in applied mechanics and engineering. 2010;199:3305-14.
[53] Belytschko T, Gracie R, Ventura G. A review of extended/generalized finite element methods for material modeling. Modelling and Simulation in Materials Science and Engineering. 2009;17:043001.
[54] Karihaloo BL, Xiao Q. Modelling of stationary and growing cracks in FE framework without remeshing: a state-of-the-art review. Computers & Structures. 2003;81:119-29.
[55] Podczeck F, Newton JM, Fromme P. The bending strength of tablets with a breaking line—Comparison of the results of an elastic and a "brittle cracking" finite element model with experimental findings. International journal of pharmaceutics. 2015;495:485-99.
[56] Bazant ZP. Fracture and size effect in concrete and other quasibrittle materials: Routledge, 2019.
[57] Zaman M, Khoury N, Solanki P. Finite-element modeling of cementitiously stabilized beams using a smeared fracture approach. International Journal of Geomechanics. 2009;9:34-42.
[58] Sabree I, Gough J, Derby B. Mechanical properties of porous ceramic scaffolds: influence of internal dimensions. Ceramics International. 2015;41:8425-32.
[59] Rao SS. Engineering optimization: theory and practice: John Wiley & Sons, 2009.
[60] Johnston I, McCluskey D, Tan C, Tracey M. Mechanical characterization of bulk Sylgard 184 for microfluidics and microengineering. Journal of Micromechanics and Microengineering. 2014;24:035017.
[61] Doyle BJ, Corbett TJ, Callanan A, Walsh MT, Vorp DA, McGloughlin TM. An experimental and numerical comparison of the rupture locations of an abdominal aortic aneurysm. Journal of Endovascular Therapy. 2009;16:322-35.
[62] Studer V, Hang G, Pandolfi A, Ortiz M, French Anderson W, Quake SR. Scaling properties of a low-actuation pressure microfluidic valve. Journal of applied physics. 2004;95:393-8.
[63] Abdullah R, Paton-Cole VP, Easterling WS. Quasi-static analysis of composite slab. Malaysian Journal of Civil Engineering. 2007;19.
[64] Li W. Damage models for soft tissues: a survey. Journal of Medical and Biological Engineering. 2016;36:285-307.
[65] Low K. Drop-impact cushioning effect of electronics products formed by plates. Advances in Engineering Software. 2003;34:31-50.
[66] Siegmund GP, Guskiewicz KM, Marshall SW, DeMarco AL, Bonin SJ. A headform for testing helmet and mouthguard sensors that measure head impact severity in football players. Annals of biomedical engineering. 2014;42:1834-45.
[67] Johnston JM, Ning H, Kim J-E, Kim Y-H, Soni B, Reynolds R, et al. Simulation, fabrication and impact testing of a novel football helmet padding system that decreases rotational acceleration. Sports Engineering. 2015;18:11-20.

[68] Tan LB, Tse KM, Lee HP, Tan VBC, Lim SP. Performance of an advanced combat helmet with different interior cushioning systems in ballistic impact: Experiments and finite element simulations. International Journal of Impact Engineering. 2012;50:99-112.
[69] Schubel PM, Luo J-J, Daniel IM. Low velocity impact behavior of composite sandwich panels. Composites Part A: Applied Science and Manufacturing. 2005;36:1389-96.
[70] Shipsha A, Hallström S, Zenkert D. Failure mechanisms and modelling of impact damage in sandwich beams-a 2D approach: part I-experimental investigation. Journal of Sandwich Structures & Materials. 2003;5:7-31.
[71] Ajdari A, Nayeb-Hashemi H, Vaziri A. Dynamic crushing and energy absorption of regular, irregular and functionally graded cellular structures. International Journal of Solids and Structures. 2011;48:506-16.
[72] Hazizan MA, Cantwell W. The low velocity impact response of an aluminium honeycomb sandwich structure. Composites Part B: Engineering. 2003;34:679-87.
[73] Sun Y, Gao L. Structural responses of all-composite improved-pyramidal truss sandwich cores. Materials & Design. 2013;43:50-8.
[74] Kao Y-T, Amin AR, Payne N, Wang J, Tai BL. Low-velocity impact response of 3D-printed lattice structure with foam reinforcement. Composite Structures. 2018;192:93-100.
[75] Dunnett CW. A Multiple Comparison Procedure for Comparing Several Treatments with a Control. Journal of the American Statistical Association. 1955;50:1096-121.
[76] Amin AR, Kao Y-T, Tai BL, Wang J. Dynamic Response of 3D-Printed Bi-Material Structure Using Drop Weight Impact Test. 2017:V002T01A21.
[77] Wang X, Jiang M, Zhou Z, Gou J, Hui D. 3D printing of polymer matrix composites: A review and prospective. Composites Part B: Engineering. 2017;110:442-58.
[78] Compton BG, Lewis JA. 3D-printing of lightweight cellular composites. Advanced materials. 2014;26:5930-5.
[79] Martin JJ, Fiore BE, Erb RM. Designing bioinspired composite reinforcement architectures via 3D magnetic printing. Nature communications. 2015;6:8641.
[80] Chabaud G, Castro M, Denoual C, Le Duigou A. Hygromechanical properties of 3D printed continuous carbon and glass fibre reinforced polyamide composite for outdoor structural applications. Additive Manufacturing. 2019;26:94-105.
[81] Gama N, Ferreira A, Barros-Timmons A. 3D printed cork/polyurethane composite foams. Materials & Design. 2019:107905.
[82] Jahangir M, Billah K, Lin Y, Roberson D, Wicker R, Espalin D. Reinforcement of material extrusion 3D printed polycarbonate using continuous carbon fiber. Additive Manufacturing. 2019;28:354-64.
[83] Singh R, Kumar R, Singh I. Investigations on 3D printed thermosetting and ceramic-reinforced recycled thermoplastic-based functional prototypes. Journal of Thermoplastic Composite Materials. 2019:0892705719864623.
[84] Boparai K, Singh R, Singh H. Comparison of tribological behaviour for Nylon6-Al-Al2O3 and ABS parts fabricated by fused deposition modelling: This paper reports a low cost composite material that is more wear-resistant than conventional ABS. Virtual and Physical Prototyping. 2015;10:59-66.

[85] Papon EA, Haque A. Fracture toughness of additively manufactured carbon fiber reinforced composites. Additive Manufacturing. 2019;26:41-52.
[86] Weng Y, Lu B, Li M, Liu Z, Tan MJ, Qian S. Empirical models to predict rheological properties of fiber reinforced cementitious composites for 3D printing. Construction and Building Materials. 2018;189:676-85.
[87] Li T, Wang L. Bending behavior of sandwich composite structures with tunable 3D-printed core materials. Composite Structures. 2017;175:46-57.
[88] Sarvestani HY, Akbarzadeh A, Niknam H, Hermenean K. 3D printed architected polymeric sandwich panels: Energy absorption and structural performance. Composite Structures. 2018;200:886-909.
[89] Li T, Chen Y, Hu X, Li Y, Wang L. Exploiting negative Poisson's ratio to design 3D-printed composites with enhanced mechanical properties. Materials & Design. 2018;142:247-58.
[90] Kim Y, Tentzeris MM, Lim S. Low-Loss and Light Substrate Integrated Waveguide Using 3D Printed Honeycomb Structure. Materials. 2019;12:402.
[91] Al-Ketan O, Soliman A, AlQubaisi AM, Abu Al-Rub RK. Nature-Inspired Lightweight Cellular Co-Continuous Composites with Architected Periodic Gyroidal Structures. Advanced Engineering Materials. 2018;20:1700549.
[92] Dalaq AS, Abueidda DW, Al-Rub RKA, Jasiuk IM. Finite element prediction of effective elastic properties of interpenetrating phase composites with architectured 3D sheet reinforcements. International Journal of Solids and Structures. 2016;83:169-82.
[93] Sabet FA, Su FY, McKittrick J, Jasiuk I. Mechanical Properties of Model Two-Phase Composites with Continuous Compared to Discontinuous Phases. Advanced Engineering Materials. 2018;20:1800505.
[94] Wang L, Lau J, Thomas EL, Boyce MC. Co-continuous composite materials for stiffness, strength, and energy dissipation. Advanced materials. 2011;23:1524-9.
[95] Mansouri M, Montazerian H, Schmauder S, Kadkhodapour J. 3D-printed multimaterial composites tailored for compliancy and strain recovery. Composite Structures. 2018;184:11-7.
[96] Yue Z, Qi J, Zhao X, Badreddine H, Gao J, Chu X. Springback Prediction of Aluminum Alloy Sheet under Changing Loading Paths with Consideration of the Influence of Kinematic Hardening and Ductile Damage. Metals. 2018;8:950.
[97] Lenkey G, Balogh Z, Hegman N. Finite element modelling of Charpy impact testing. Transferability of fracture mechanical characteristics: Springer; 2002. p. 291-302.
[98] Song Y, Li Y, Song W, Yee K, Lee K-Y, Tagarielli V. Measurements of the mechanical response of unidirectional 3D-printed PLA. Materials & Design. 2017;123:154-64.
[99] Widdle Jr R, Bajaj A, Davies P. Measurement of the Poisson’s ratio of flexible polyurethane foam and its influence on a uniaxial compression model. International Journal of Engineering Science. 2008;46:31-49.